

1 **Phytoplankton tune local pH to actively modulate circadian swimming behavior**

2

3 Arkajyoti Ghoshal<sup>1</sup>, Jayabrata Dhar<sup>2</sup>, Hans-Peter Grossart<sup>3,4</sup>, and Anupam Sengupta<sup>1\*</sup>

4 <sup>1</sup>Physics of Living Matter Group, Department of Physics and Materials Science, University of  
5 Luxembourg, 162A, Avenue de la Faïencerie, L-1511 Luxembourg City, Luxembourg

6 <sup>2</sup>Department of Mechanical Engineering, National Institute of Technology Durgapur, 713203, India

7 <sup>3</sup>Department of Plankton and Microbial Ecology, Leibniz Institute of Freshwater Ecology and Inland  
8 Fisheries, Zur alten Fischerhuette 2, 16775 Stechlin, Gemany

9 <sup>4</sup>Institute of Biochemistry and Biology, Potsdam University, Maulbeerallee 2, D-14469 Potsdam,  
10 Germany

11

12 \* To whom correspondence should be addressed: [anupam.sengupta@uni.lu](mailto:anupam.sengupta@uni.lu)

13

14 **One sentence summary:** Active regulation of local pH diversifies the diel vertical migration  
15 of motile phytoplankton.

16 **Funding:** This work was supported by the Luxembourg National Research Fund's AFR-Grant  
17 (Grant no. 13563560) and the ATTRACT Investigator Grant, A17/MS/11572821/MBRACE,  
18 to A.S. Support from the German Science Foundation project (DFG, Pycnotrap GR1540/37-1  
19 to H-P.G.) is gratefully acknowledged.

20 **Author contributions:** A.S. developed the research plan and directed all parts of the project.  
21 A.G. carried out experiments, analyzed the data and ran the statistical tests. A.G, J.D., and A.S.  
22 prepared figures. J.D and A.S. set up the single-cell biomechanics model; J.D. carried out  
23 computations and compiled the phase maps with directions from A.S. H.P.G. contributed to  
24 discussions and data interpretation. A.G. and A.S. wrote the paper with inputs from all authors.

25 **Acknowledgements:** The authors thank Robert Himelrick and Nicolas Tournier for the  
26 support with fabrication of experimental chambers.

27 **Competing interests:** Authors declare no competing interests.

28 **Data and materials availability:** Data and codes are available in the main text, or upon  
29 requests to the corresponding author.

30 **Keywords:** phytoplankton, circadian rhythm, diel vertical migration, gravitaxis, pH,  
31 reorientation, morphology, photophysiology

32

33

34

35

36

37

## 38 **Abstract**

39 Diel vertical migration (DVM), the diurnal exodus of motile phytoplankton between the light-  
40 and nutrient-rich aquatic regions, is governed by endogenous biological clocks. Many species  
41 exhibit irregular DVM patterns wherein out-of-phase gravitactic swimming—relative to that  
42 expected due to the endogenous rhythm—is observed. How cells achieve and control this  
43 irregular swimming behavior, and its impact on biological fitness remain poorly understood.  
44 Combining local environmental monitoring with behavioral and physiological analyses of  
45 motile bloom-forming *Heterosigma akashiwo* cells, we report that phytoplankton species  
46 modulate their DVM pattern by progressively tuning local pH, yielding physiologically  
47 equivalent yet behaviorally distinct gravitactic sub-populations which remain separated  
48 vertically within a visibly homogeneous cell distribution. Individual and population-scale  
49 tracking of the isolated *top* and *bottom* sub-populations revealed similar gravitactic (swimming  
50 speed and stability) and physiological traits (growth rate and maximum photosynthetic yield),  
51 suggesting that the sub-populations emerge due to mutual co-existence. Exposing the top  
52 (bottom) sub-population to the spent media of the bottom (top) counterpart recreates the  
53 emergent vertical distribution, while no such phenomenon was observed when the sub-  
54 populations were exposed to their own spent media. A model of swimming mechanics based  
55 on the quantitative analysis of cell morphologies confirms that the emergent sub-populations  
56 represent distinct swimming stabilities, resulting from morphological transformations after the  
57 cells are exposed to the spent media. Together with the corresponding night-time dataset, we  
58 present an integrated picture of the circadian swimming, wherein active chemo-regulation of  
59 the local environment underpins motility variations for potential ecological advantages via  
60 intraspecific division of labor over the day-night cycle. This chemo-regulated migratory trait  
61 offers mechanistic insights into the irregular diel migration, relevant particularly for modelling  
62 phytoplankton transport, fitness and adaptation as globally ocean waters see a persistent drop  
63 in the mean pH.

64

## 65 **Introduction**

66 Driven by the diurnal variation of light cues, phytoplankton show a periodic migratory  
67 behavior whereby they swim up to the photon-rich upper layers of the ocean during the day  
68 and swim down to the nutrient-rich deeper waters at night [1-3]. The ability to execute this  
69 diel vertical migration (DVM) over a 24 h day-night cycle is a fundamental trait of motile  
70 photosynthetic phytoplankton species. In combination with changes in the nutrient and the  
71 hydrodynamic conditions, DVM is critical for the fitness, succession and adaptation of  
72 phytoplankton to fluctuations in their environment, tailoring ecological niches suitable for  
73 microorganisms with diverse phenotypic spectrum [4-7]. Light and its gradient are key  
74 determinants of phytoplankton behavior and physiology, they impact both the swimming  
75 direction (against or toward the gravity vector) and the stability of the swimming motion  
76 under dynamic environmental conditions [8, 9]. Non-uniform distribution of light can further  
77 impact phytoplankton swimming, even drive populations off their regular DVM patterns [6].  
78 An interplay of the intrinsic circadian rhythm and local environmental factors can engender  
79 asynchronous vertical migration and distribution of motile phytoplankton [10-12]. Recent  
80 studies have shown that phytoplankton actively employ exquisite mechanisms to adapt their  
81 gravitactic swimming across diverse timescales, for instance as a response to turbulent cues  
82 [7, 13] or under long-term nutrient limitation [14].

83 Vertical migration and photophysiology of phytoplankton are intrinsically coupled, mediated  
84 by the internal levels of biochemicals including nitrate, carbon and other secondary  
85 metabolites, which in turn affect the propensity of vertical swimming [10, 12]. Depending on  
86 the species at hand, vertical migration is impacted by factors including photoacclimation [15],  
87 swimming speed [16], and the assimilation and regulation of nutrients by the phytoplankton  
88 species [17]. This characteristic diel migratory behavior of phytoplankton, known to originate  
89 solely due to changes in the light intensity, has also been reported in the deep seas where light  
90 is absent [18]. Thus, phytoplankton DVM is regulated by a combination of external light cues  
91 and endogenous circadian clock, as demonstrated in the case of the model unicellular species,  
92 *Chlamydomonas reinhardtii* [19]. Endogenous periodicity associated with phototaxis and  
93 nitrogen metabolism [19, 20] were reported, indicating the presence of circadian genes, both  
94 at the level of mRNA [21, 22] as well as DNA [23]. These studies show that periodic  
95 response can occur due to a variety of factors, even in the absence of a light cue. Yamazaki  
96 and Kamykowski's model [12, 24], based on cross-talks between the internal (chemical) state  
97 and changes in the light environment, suggest emergence of irregular migratory patterns and  
98 their potential adaptive advantages, particularly when nutrient availability (nitrate) changes.  
99 This model successfully explains DVM in the framework of decision-making, providing  
100 insights into the irregularities in phytoplankton migration, observed both in the lab and in  
101 field [2, 25, 26].

102 By controlling several internal factors, phytoplankton may 'decide' how to respond to a  
103 particular cue [11, 12]. Ideally such active decision-making could assist phytoplankton to  
104 either escape a hostile environment [7], or utilize the resources available optimally [14, 27],  
105 thereby ensuring adequate fitness. Studies investigating the nature, cause and the effects of  
106 such active decision making—leading to out-of-phase DVM patterns—are missing this far. Lab-  
107 based experiments [3, 28, 29], and proposed models have attempted to establish the decision-  
108 based vertical migration of phytoplankton [12], however the mechanistic underpinnings  
109 remain unknown. While irregular migratory behavior may potentially compromise cellular  
110 photosynthesis, it may still be physiologically beneficial over different timescales and under  
111 different environmental settings [12, 24]. Currently, the cost-to-benefit tradeoffs of irregular  
112 DVM patterns remain to be assessed, thus leaving open a fundamental gap in our  
113 understanding of this long-observed trait, and its potential ecological role as an alternative to  
114 the circadian DVM patterns.

115 Here, using *Heterosigma akashiwo* (HA), a harmful algal bloom forming raphidophyte [30-  
116 32] as a model organism, we report that phytoplankton species modulate their DVM pattern  
117 by progressively tuning the local pH, generating behaviorally distinct gravitactic sub-  
118 populations which localize at the upper (*top* sub-population) and lower (*bottom* sub-  
119 population) regions of the cell culture. The sub-populations remain vertically separated when  
120 they are co-existing, however, in isolation, the sub-populations possess similar behavioral  
121 (swimming speed and stability) and physiological traits (growth rate and maximum  
122 photosynthetic yield), suggesting that the sub-populations emerge due to mutual co-existence.  
123 We confirm this by exposing each of the sub-populations to the spent media of their  
124 counterpart, recreating the observed vertical distribution; and through single-cell imaging, we  
125 identify morphological transformations of the cells as the cause for the distinct vertical  
126 distributions. A model of swimming mechanics reveals distinct swimming stabilities which  
127 emerge due to the morphological transformations after the cells are exposed to the spent

128 media. The night-time data set confirmed that the sub-populations switch their behavioral and  
129 physiological traits (relative to the day-time values), indicating that phytoplankton actively  
130 chemo-regulate their local environment to promote intraspecific division of labor over a 24 h  
131 time window.

132

## 133 **RESULTS**

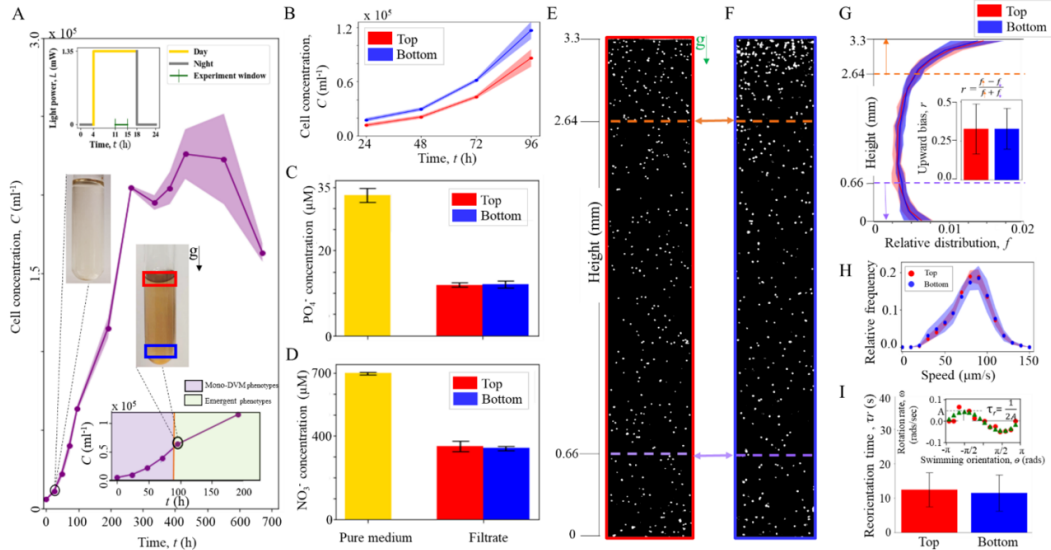
### 134 **Sub-populations with similar phenotypes yet distinct swimming properties emerge** 135 **within phytoplankton cell culture**

136 We grew *Heterosigma akashiwo* CCMP452 (henceforth referred to as HA452) in culture  
137 tubes under 14:10 day: night cycle and uniform light conditions (Materials and Methods, Fig.  
138 1A inset, top-left). The cell cultures used here originate from a monoclonal culture, which are  
139 propagated for multiple generations as continuous cultures. For the propagation, cells from  
140 the top 0.5 mm of the mother culture are collected and put in a fresh nutrient-rich medium to  
141 grow (Materials and Methods). To check if the cells grow optimally, we extracted the growth  
142 curve by measuring the cell numbers using microscopy and image processing, and compared  
143 it with previously reported growth curves of HA452 [7, 14]. The computed cell concentration  
144 is plotted as a function of time and shown in Fig. 1A, B. From this growth curve, the  
145 doubling time is calculated (Fig. S1), which turns out to be  $26 \pm 2$  h, indicating that the cells  
146 have optimum growing conditions. The bottom-left inset of Fig. 1A shows a typical culture  
147 tube at 96 hours of growth, imaged during daytime (11 h). We observe that, despite optimal  
148 growth conditions and absence of any external stimulus, cells distribute all along the vertical  
149 height of the culture tube rather than confining only at the top, as expected from their diel  
150 migratory behavior [3, 32]. The light field in all our experiments are maintained uniform in  
151 all our experiments. While irregular patterns of DVM are known, they are usually in response  
152 to fluctuations in the environment, mostly in terms of nutrient availability. Naturally, we  
153 wanted to investigate if the distribution of nutrients along the culture tube is uniform or not.  
154 We collected cell suspensions from the top and bottom of the culture tubes at 96 h, filtered  
155 out the cells and computed the nitrate and phosphate concentrations (the two most crucial  
156 nutrients reported in irregular DVM) of the filtrate (Fig. 1C, D). The detailed steps of  
157 generating cell filtrate are shown in Fig. S2 and the same protocol is used for all experiments  
158 mentioned. We noted that there was no major difference between the concentrations of either  
159 nutrient across top and bottom samples (Fig. 1C, D). In case of a pure medium, that formed  
160 our control (Fig. 1C, D, left panel), there was also no difference between top and bottom  
161 samples, and showed comparable growth rates (Fig. 1C) suggesting homogeneous  
162 distribution. Even though there was no notable difference across samples from growing  
163 culture, it is to be noted that the overall nutrient levels went down (as compared to pure  
164 medium). This is due to active consumption by growing and dividing cells and the pattern of  
165 depletion was similar to other *H. akashiwo* strains [14]. Also, this points to the fact that even  
166 with cells present, distribution of nutrients remains homogeneous. We hypothesized that a  
167 difference in swimming behavior can lead to the emergence of spatial segregation even under  
168 DVM, for example directionally stable cells or cells with higher swimming speeds will be  
169 able to swim up/down and occupy these regions before the others. Towards this, we collected  
170 cells from top and bottom and investigated key static and dynamic motility parameters. First,  
171 we wanted to see the steady-state vertical distribution of top vs bottom cell samples (static

172 parameter). We put the cell suspensions in a milli-fluidic chamber, referred to as ‘small  
173 chamber’ henceforth, (10mm x 3.3 mm x 2mm) and let them acclimatize for 20 min., and  
174 captured the distribution from short real time videos (Fig. 1E, F). The image analysis pipeline  
175 to obtain these parameters from raw data is shown in the supplementary Fig. S2. The  
176 individual vertical distribution profile for each replicate of both sub-populations is shown in  
177 Fig. S4 A, B. Ideally, cells collected from the top of the culture tube should mostly be  
178 swimming to the top of the chamber and vice versa. We analyzed the frames to obtain  
179 individual cell centroid coordinates and arranged them to numerically represent the vertical  
180 distribution seen in the frames (Fig. 1G). We then quantified the distribution using a metric  
181 called *upward bias index*, as described by Sengupta *et. al.* [7] (Fig. 1G, inset),  $r = (f \uparrow - f \downarrow)$   
182  $)/(f \uparrow + f \downarrow)$  where  $f \uparrow$  and  $f \downarrow$  are the cell concentration in the top and bottom of an  
183 observation window. In our case, we defined them to be the top and the bottom 1/5<sup>th</sup> of the  
184 chamber height (660  $\mu\text{m}$ ), shown by orange and lavender lines (Fig. 1E-G). For top samples,  
185 the mean  $r$  ( $\pm$  standard deviation) value across all replicates is  $0.33 \pm 0.16$  and for bottom  
186 ones, it is  $0.33 \pm 0.13$ . Both the distribution pattern and the  $r$  values suggest that the behavior  
187 of top and bottom cells in isolation is identical in terms of vertical distribution i.e., under the  
188 same relaxation time, i) majority of cells in both samples swim up ( $r > 0$ ), ii) bottom cells can  
189 swim up just as well as top cells (comparable  $r$  values) and iii) not all cells collected from the  
190 top of the culture tube can make it to the top of the small chamber ( $r < 1$ ). One possibility is  
191 that the relaxation time is large enough for cells in both the samples to swim to the top even  
192 though they have naturally different swimming speeds. To test this, we quantified the speeds  
193 by flipping the small chamber by 180 degrees after 20 min. of relaxation time. As we saw  
194 from the vertical distribution, most of the cells had swam to the top of the small chamber and  
195 formed their steady-state distributions (Fig. 1G). Cells reaching the top must be strongly  
196 negatively gravitactic and after a 180 degree flip, they are at the bottom of the chamber and  
197 will naturally try to swim to the top, giving us quantitative insights into the swimming  
198 behavior (revealed by the trajectories). Note that this is true for all other cells of a sample as  
199 well, not just negatively gravitactic ones. Less negatively gravitactic cells will be present  
200 towards the bottom of the chamber and vice versa and contribute to the complete steady state  
201 distribution of the sample. We analyzed the trajectories (Materials and Methods) of both  
202 samples to obtain the mean ( $\pm$  standard deviation) absolute speeds for the top ( $85.6 \pm 21.5$   
203  $\mu\text{m/s}$ ) and bottom ( $86.7 \pm 23 \mu\text{m/s}$ ) as shown in Fig. 1H. The samples show no significant  
204 difference, and speed can be ruled out as a major factor to trigger opposite gravitactic  
205 behavior. We also computed the  $x$ - and  $y$ - velocity components for both the samples (Fig.  
206 S5). There is no notable difference, indicating that the swimming pattern of both samples are  
207 similar. The preferred direction of swimming of a cell depends on the stability of the cell  
208 towards or away from gravity vector (biophysically speaking) and difference in stability can  
209 govern the physical location of cells along the vertical and hence the final distribution. To test  
210 this, we computed the orientational stability of top and bottom samples, with respect to the  
211 negative gravity vector (Fig. 1I). The individual plots for each replicate of both sub-  
212 populations is shown in Fig. S6 A, B. Stability is quantified in terms of reorientation time,  $\tau_r =$   
213  $1/2A$  ( $A$  being the stability parameter obtained by plotting the instantaneous rotation rate,  $\omega$ ,  
214 as a function of the instantaneous angular position,  $\theta$ . which, for the top sub-population is  
215  $12.2 \pm 4.9$  s and  $11.48 \pm 5.3$  s for the bottom counterpart. These findings confirm that under  
216 uniform growth conditions, cells show identical behavior in isolation, however this does not  
217 explain the collective behavior within a cell culture. One factor could be that some cells are

218 better at sustained up-swimming (over longer vertical distances) and others not, thus some are  
 219 programmed to stay up and vice versa. We test this hypothesis next by studying the  
 220 swimming behavior within a taller vertical chamber, described in the following section.

221



222

223 **Fig. 1. Vertically segregated sub-populations, with similar behavioral traits, emerge at the top**  
 224 **and bottom regions of a homogeneous cell culture. (A)** Growth curve of *Heterosigma akashiwo* (HA)  
 225 452 culture (number of replicates,  $n = 4$ ), grown under a 14 h (light) – 10 h (dark) cycle (inset, top-left)  
 226 at 22°C within a vertical culture column is ~70mm. The inset (bottom-right) marks the timepoint at  
 227 which the vertically segregated sub-populations emerge, visualized by the uniform hue of the  
 228 homogeneous cell culture (upper inset panel of culture at 96 h after inoculation), compared to the  
 229 vertical gradient of hue observed for the negatively gravitactic cell population (before 96 h). The darker  
 230 hue on the upper part of the culture and lighter below indicate the presence of higher number of cells  
 231 near the top. **(B)** Growth curves of the top (red) and bottom (blue) sub-populations, after they have been  
 232 isolated from the mother culture, show similar trends relative to each other, and with that of the original  
 233 culture (shown in panel **(A)**). The error (s.d.) is shown by the shaded portion of the plot. **(C, D)**  
 234 Spectrophotometric analysis of the pure and spent media (96 h after inoculation) reveals comparable  
 235 nitrate **(C)** and phosphate **(D)** concentrations present in the top (red) and bottom (blue) sub-populations.  
 236 Yellow bar indicates nutrient levels of a pure medium. The plots show mean ( $\pm$  s.d.) for 2 biological  
 237 replicates per sample. **(E)** Stationary distribution of the HA452 cells isolated from the top and bottom  
 238 **(F)** sub-populations within a vertical chamber (height ~3.3 mm, bright spots indicate cells, shown after  
 239 subtraction of the background intensity) after 20 minutes of equilibration time. The gravity vector is  
 240 indicated by **g**. **(G)** Stationary vertical distribution obtained from all frames of video micrography,  
 241 shown over the chamber height for top ( $n = 6$ , average cell count per replicate,  $N = 1356 \pm 283$ ) and  
 242 bottom ( $n = 6$ ,  $N = 1757 \pm 734$ ) sub-populations. Inset shows comparable upward bias index,  $r = (f_{\uparrow} -$   
 243  $f_{\downarrow}) / (f_{\uparrow} + f_{\downarrow})$  for each case, where  $f_{\uparrow}$  and  $f_{\downarrow}$  are the concentrations of cells within the first and the last  
 244 660  $\mu\text{m}$  of the chamber, indicated by the arrow heads next to the dashed lines up ( $\uparrow$ , dark orange) and  
 245 down ( $\downarrow$ , lavender) in panels **(E)** and **(F)**. **(H)** Relative distribution of swimming speeds of the sub-  
 246 populations, obtained by analyzing swimming trajectories (after flipping the chamber by 180 degrees),  
 247 shows similar motility ( $n = 6$ ,  $N = 670 \pm 122$ , speed =  $85.6 \pm 21.5 \mu\text{m/s}$ ) and bottom ( $n = 6$ ,  $N = 829 \pm$   
 248  $421$ , speed =  $86.7 \pm 23 \mu\text{m/s}$ ). **(I)** Swimming stability measured as the reorientation timescale,  $\tau_r$ ,  
 249 (inversely proportional to swimming stability) of the top ( $n = 12$ ,  $N = 586 \pm 133$ ) and bottom ( $n = 12$ ,  
 250  $N = 742 \pm 255$ ) sub-populations are shown respectively as red and blue bar plots. For each cell  
 251 undergoing reorientation, trajectory is analyzed to find out instantaneous angular direction of swimming

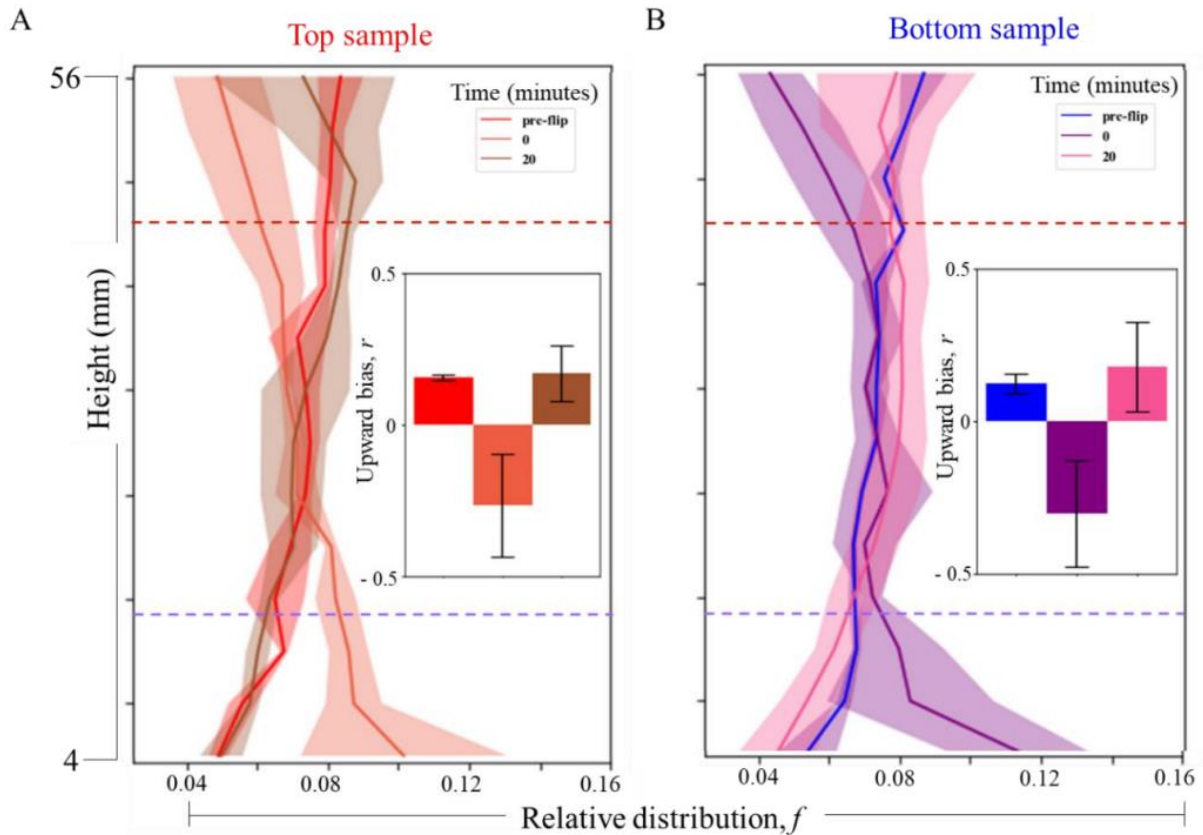
252  $\langle \theta \rangle$  and the instantaneous rotational rate ( $\omega$ ) is plotted against  $\theta$  to obtain a curve shown by red dots in  
253 the inset. This is then fitted to a sinusoidal curve (green dots), the peak of which is the maximum rotation  
254 rate,  $A$ , and  $\tau_r = \frac{1}{2A}$ . The mean reorientation timescales for the top and the bottom sub-populations are  
255  $12.8 \pm 5$  s and  $11.5 \pm 5$  s respectively.

## 256 **Swimming behavior of sub-populations remains consistent over longer vertical distance**

257 In oceans, diverse phytoplankton species can grow up to depths of tens up to hundred meters  
258 below the sea surface [33-35]. Swimming over large distances can be energetically costly,  
259 thus it is imperative to observe if phytoplankton alter their swimming behavior over longer  
260 vertical distances. Specifically, it would be relevant for us to check if, and how the swimming  
261 speeds of cells from the top and bottom sub-populations emerge over time, as they swim over  
262 larger vertical distances (over shorter distances, no difference was observed as reported in  
263 Fig. 1). We use a ‘tall chamber’ with a vertical height of 60 mm (Fig. 2A, see Materials and  
264 Methods section), comparable to the entire vertical depth that the cells experience within the  
265 culture tubes (the height of the culture is  $\sim 70$  mm), and measure the vertical distribution of  
266 sub-populations over time. Cells collected from the top and the bottom 0.5 mm of a culture  
267 tube were introduced to the tall chamber and allowed  $\sim 20$  min. to acclimatize within it,  
268 forming a steady distribution. Considering an average swimming speed of  $85 \mu\text{m/s}$  for either  
269 sub-population, a cell with an average swimming speed would ideally reach from one end to  
270 the other (distance of 60 mm) in roughly 12 min. So, the waiting time of 20 min. should be  
271 sufficient for the strongly negative gravitactic cells to reach the top of the chamber.  
272 Thereafter, the chamber was flipped instantaneously, allowing cells to reorient and swim up  
273 against the gravity. After the flip, the entire chamber was imaged immediately (time,  $t = 0$   
274 min.) with a custom-built series-connected translation stage allowing long distance  
275 movements (Materials and Methods). Then, another 20 min. were allowed before imaging the  
276 chamber again ( $t = 20$  min.). The imaging was done without the first and last 4 mm as these  
277 regions were too close to the inlet ports, where cell counting was technically challenging.  
278 Cell distribution was considered within the remaining 52 mm (dotted line, Fig. 2A). Figure  
279 2A, B show the distributions at 0 and 20 min. post-flip, for the top and the bottom sub-  
280 populations respectively. Once again, we found that the vertical distributions of the sub-  
281 populations in the tall chamber appear statistically comparable, indicating that the bottom  
282 sub-population, in isolation, have similar swimming characteristics as their top counterparts,  
283 even over long distances.

284 The similarity of swimming traits is also confirmed by the upward bias values as plotted in  
285 the insets of Fig. 2A, B ( $r = 0.17 \pm 0.1$  for top, and  $0.18 \pm 0.15$  for the bottom sub-  
286 populations). Taken together, the results indicate that, when isolated, cells from the bottom  
287 sub-population can effectively swim up like the top ones, even over longer distances. Since  
288 we do not see this occur in the culture tubes, we infer that either (i) the fluxes of the top and  
289 bottom sub-populations maintain a dynamic equilibrium, shuttling continuously across the  
290 entire culture tube; or (ii) when the top and the bottom sub-populations co-exist, difference in  
291 the swimming properties emerge, relative to those in isolation. Continuous swimming to  
292 maintain a dynamic equilibrium within the cell culture is an energetically expensive option,  
293 particularly under the uniform light and nutrient conditions present in our experiments. Thus,  
294 we focus on the second possibility that distinct swimming properties emerge when the sub-  
295 populations co-exist. In the following sections, we delineate how the top and bottom

296 swimmers emerge, and provide a mechanistic understanding of this behavior, commensurate  
 297 with other physiological markers including photophysiology over both day and night-times.



298

299 **Fig. 2. Distinct gravitactic sub-populations emerge also in longer vertical columns. (A)** Mean  $\pm$  s.d.  
 300 of the vertical distribution of the top subpopulation within a 60 mm tall chamber, imaged 20 min after  
 301 the chamber is filled (pre flip,  $n = 2$ ,  $N = 35503 \pm 383$ , red line). The chamber is then rotated by 180  
 302 degrees along the vertical plane, the distribution is recorded immediately thereafter (post flip, 0 minutes,  
 303  $n = 3$ ,  $N = 27666 \pm 3091$ , orange line); and after 20 minutes (post flip, 20 minutes,  $n = 3$ ,  $N = 32563 \pm$   
 304  $1070$ , brown line). The inset compares the upward bias,  $r$ , from the corresponding distributions (mean  
 305  $\pm$  s.d.). At  $t = 20$  min, pre flip,  $r = 0.157 \pm 0.01$ ; at  $t = 0$  min post flip,  $r = -0.265 \pm 0.17$ ; and 20 min  
 306 after flip,  $r = 0.17 \pm 0.1$ . **(B)** Mean  $\pm$  s.d. of the vertical distribution of the bottom subpopulation within  
 307 the 60 mm tall chamber, imaged 20 min after the chamber is filled (pre flip,  $n = 2$ ,  $N = 35552 \pm 922$ ,  
 308 blue line). The chamber is then rotated by 180 degrees along the vertical plane, the distribution is  
 309 recorded immediately thereafter (post flip, 0 minutes,  $n = 4$ ,  $N = 31234 \pm 5560$ , purple line); and after  
 310 20 minutes (post flip,  $n = 3$ ,  $N = 31483 \pm 5785$ , magenta line). The inset compares the upward bias,  $r$ ,  
 311 obtained from the corresponding distributions (mean  $\pm$  s.d.). At  $t = 20$  min, pre flip,  $r = 0.126 \pm 0.03$ ;  
 312 at  $t = 0$  min post flip,  $r = -0.3 \pm 0.18$ ; and 20 min after flip,  $r = 0.18 \pm 0.15$ .

313

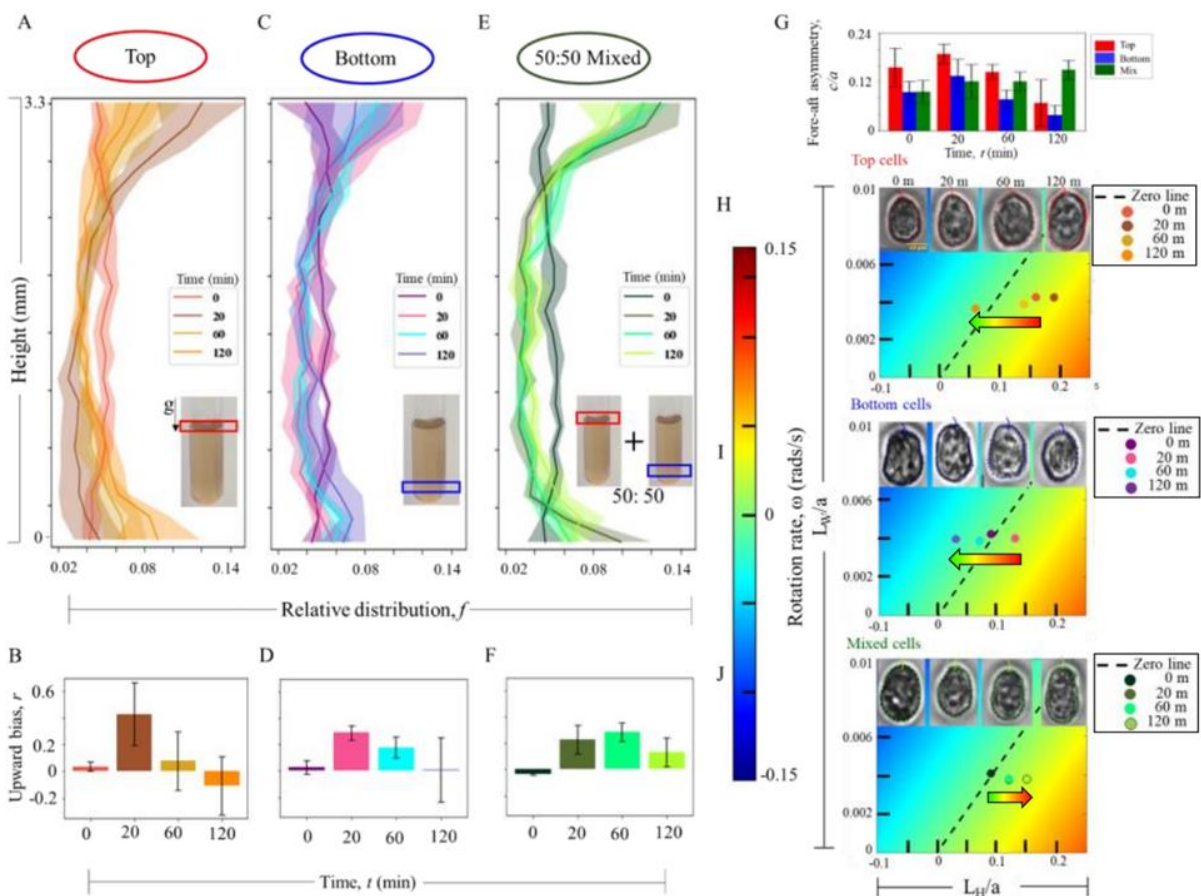
### 314 Co-existence alters swimming behavior of sub-populations via morphological changes

315 We observe the vertical distribution of each sub-population over a long time (120 min.), and  
 316 compare this distribution of a mixed population (50:50) over the same time span. A timescale  
 317 of 120 min. should be sufficient to observe any behavioral change that can alter changes in  
 318 the vertical distribution (reorientation timescale  $\sim 10$  s, with swimming speed of average 85  
 319  $\mu\text{m/s}$ , cells take  $\sim 40$  s to cover the vertical span of the short chamber (3.3 mm), adaptive



320 response to external stimuli  $\sim 10$  s of seconds [7, 13, 36]. Fig. 3 A, C and E plot the vertical  
 321 distribution over time for the isolated (top and bottom) sub-populations and their 50:50  
 322 mixture. Our results confirm that the top (Fig. 1A) and bottom (Fig. 1B) sub-populations  
 323 show similar vertical distributions over time, for the entire observation window (Fig. 3 B, D).  
 324 Starting with a uniform distribution at  $t = 0$  min., cells occupy the upper parts of the  
 325 chambers at  $t = 20$  min., confirming the behavior reported in Figs. 1 and 2. Over longer  
 326 durations, cells start to swim downward, reaching  $r \sim 0$  (or  $< 0$ , upward bias values) at  $t = 120$   
 327 min. While the trends we observe for the top and bottom sub-populations are similar, the rate  
 328 of change of the upward bias,  $r$ , are different, with the bottom sub-populations showing a  
 329 relatively lower rate of change compared to the top sub-population. When both sub-  
 330 populations are mixed, mimicking the co-existence case, the vertical distribution pattern  
 331 emerges slowly, with  $r$  remaining positive during the entire duration of observation (Fig. 3F).  
 332 This indicates that cells from a sub-population, in presence of its complementary counterpart,  
 333 tend to maintain the vertical segregation (indicated by the positive  $r$  values). In contrast, the  
 334 isolated sub-populations switched their equilibrium swimming direction downward (Fig. 3B, D).  
 335 Overall, we conclude that, in isolation, cells from both the sub-populations show similar  
 336 swimming behavior, equilibrating to low  $r$  values over long time; whereas under co-  
 337 existence, the mixed population maintains a significant positive  $r$  value over long times.

338



339

340 **Fig. 3. Coexistence of sub-populations triggers spontaneous alteration of cell morphology and**  
 341 **swimming stability.** Vertical distribution over time spanning 0 min., 20 min., 60 min., and 120 min.,  
 342 for the (A) top;  $n = 4$ ,  $N = 1146 \pm 205$ , (C) bottom;  $n = 4$ ,  $N = 947 \pm 306$ , and (E) 50:50 mixed;  $n = 4$ ,  
 343  $N = 1079 \pm 246$  populations of cells.  $t = 0$  min corresponds to start of the imaging immediately after the

344 chamber was filled. The corresponding upward bias values ( $r$ ) over time is shown in panels (B), (D),  
345 (F). (G) Morphological analysis of single cells reveal change in the fore-aft shape asymmetry over time  
346 (indicated by the value of  $c/a$ ) for the three cases; bar plots show mean  $\pm$  s.d. (H). Single cells were  
347 imaged in each case ( $N = 10$ ), from which the cell contours were extracted and fitted to a mathematical  
348 curve (Materials and Methods) to obtain cell size parameter,  $b/a$  and the fore-aft asymmetry parameter,  
349  $c/a$ , where  $a$ ,  $b$  and  $c$  are the major, minor axes and degree of fore-aft asymmetry respectively. A cell  
350 mechanical model captures the emerging variation of swimming stability (orientational stability) over  
351 time, as  $L_H/a$  and  $L_W/a$  values change.  $L_H$  is the distance between the centre of buoyancy and the  
352 centre of hydrodynamic stress, while  $L_W$  is that between the centre of buoyancy and the centre of mass  
353 (see Materials and Methods). Varying one with respect to the other alters the orientational stability of  
354 the swimming cell, which is captured by the rotation rate,  $\omega$ :  $\omega > 0$  ( $< 0$ ) indicates cells which are stable  
355 against (toward) the gravity direction;  $\omega = 0$  indicates neutrally stable cells with no preferred direction  
356 of orientation (dotted black line). When isolated, the orientational stability of the top and the bottom  
357 sub-populations reduces over time (arrow indicates leftward as time increases, top and middle panels),  
358 whereas for the mixed sample, orientational stability increases over time, while remaining positive  
359 throughout (bottom panel). The insets at the top of each panel show representative single cell images  
360 for each case, obtained using phase contrast microscopy.

361

362 To find the mechanistic underpinnings of the difference in the swimming trends, we  
363 quantified the morphology of the cells from each of the experimental samples. Morphology is  
364 a key parameter that determine the swimming stability and any difference therein, that could  
365 alter the swimming direction. At  $t = 0$  min. (reflecting the native morphological state of the  
366 cells, similar to those in the culture tube), cells from top sub-population show a high degree  
367 of fore-aft asymmetry ( $c/a$ ) compared to the bottom or mixed cases (Fig. 3G, H). Higher  $c/a$   
368 indicate high degree of fore-aft asymmetry, resulting in strongly negative gravitactic  
369 swimming properties, and vice versa. As time elapsed, the  $c/a$  value increased for both the  
370 top and bottom sub-populations (Fig. 3H, top and middle panels), reaching  $0.19 \pm 0.3$  for the  
371 top cells, and  $0.14 \pm 0.5$  for the bottom cells. This indicates that cells—over short time scales  
372 following the transfer to the millifluidic device—increased negative gravitactic ability, a  
373 signature of the reduction of the physiological stress [7, 13]. At 60 min., both the bottom and  
374 the top cells start to get symmetric in morphology ( $c/a$  lowers to  $0.14 \pm 0.02$  and  $0.08 \pm 0.03$   
375 respectively), with the trend continuing during the entire course of our experiments (120  
376 min.). At 120 min, cells from both sub-populations attain similar  $c/a$  values ( $0.07 \pm 0.06$  and  
377  $0.04 \pm 0.02$ ), confirming that, in isolation, the top and bottom sub-populations have  
378 comparable morphotypes (Fig. S7, S8). While the top and bottom sub-populations exhibit  
379 similar variation of fore-aft asymmetry with time, the top cells, relatively, are more elliptical  
380 than the bottom ones, as captured by the  $b/a$  values (Fig. S10). Consequently, this results in  
381 an overall decrease in the swimming stability over time, as shown in the phase plots (Fig. 3H,  
382 upper and middle panels).

383 In the mixed population scenario (a 50:50 mixture of top and bottom sub-populations), the  
384 initial fore-aft asymmetry ( $c/a = 0.10 \pm 0.04$ ) was lower than that in each of the individual  
385 sub-populations. The cells show a slight increase in the  $c/a$  value ( $0.12 \pm 0.04$  at  $t = 20$  min.),  
386 reaching up to  $0.15 \pm 0.04$  by 120 min. With respect to the individual sub-populations, the  
387 observed trend – an overall increase of the fore-aft asymmetry – is opposite, as also  
388 corroborated by the vertical distribution, and the swimming stability captured by our  
389 computational fluid dynamical model (Fig. 3H, lower panel). Statistically, the overall change

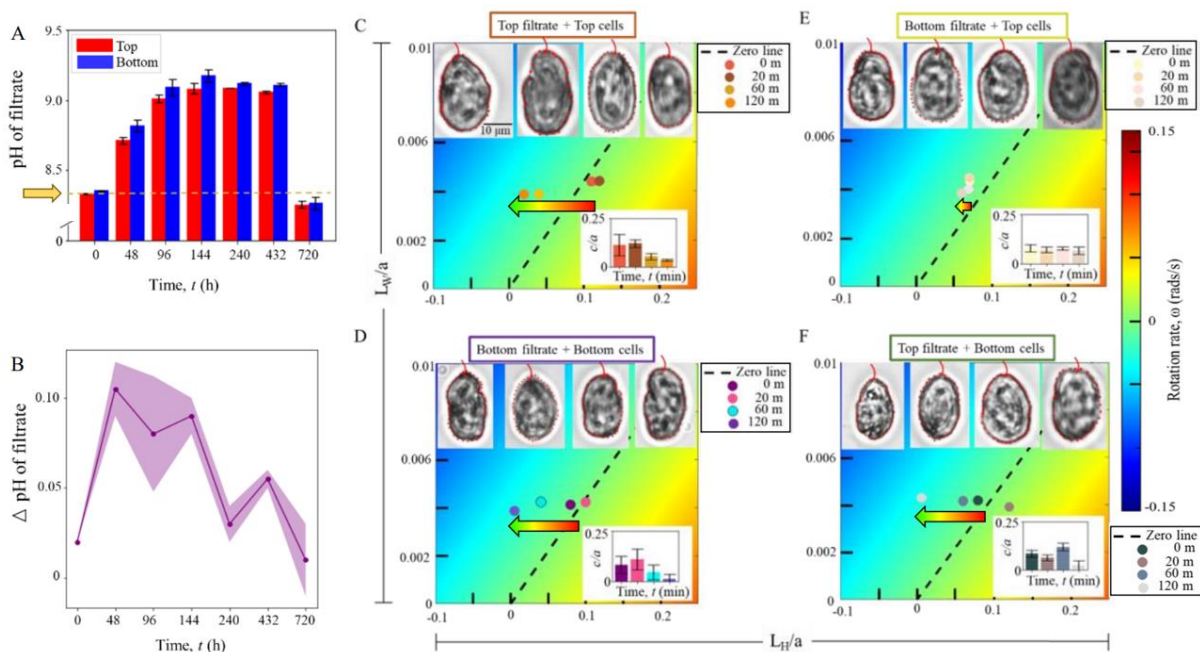
390 in the population fore-aft asymmetry could arise due to the increase of  $c/a$  values in some  
 391 cells, and lowering in others, effectively retaining a uniform value (Fig. S9). Furthermore,  
 392 this indicates an emergent stability, supported by the data obtained at 20 min: the  $c/a$  of  
 393 mixed population is lower than that of the average value of the top and bottom sub-  
 394 populations, thus showing that the stability of the mixed population is not simply a  
 395 superposition of the swimming stabilities of the individual components. From this we can  
 396 conclude that under co-existence, the mixed population shows a distinct swimming stability  
 397 and vertical distribution, otherwise not observed under isolated conditions.

398

### 399 **Phytoplankton chemo-regulate local pH to diversify the circadian swimming behavior**

400 The distinct alteration of the cell morphology in the 50:50 mixture, relative to the isolated  
 401 sub-populations, indicates that cells in the mixture experience physiological stress that trigger  
 402 morphological changes, ultimately impacting the swimming behavior [7, 13]. We identify the  
 403 local pH, and the relative difference between the pH of the spent media associated with the  
 404 top and the bottom sub-populations, as the driver of the reported observations (Fig. 4 A). As  
 405 the population grows, the pH of the cell culture increased from  $8.72 \pm 0.03$  (top,  $8.82 \pm 0.04$   
 406 for bottom)  $\sim 48$  h after inoculation, to  $9.01 \pm 0.02$  ( $9.09 \pm 0.06$  for bottom) at  $\sim 96$  h.  
 407 Thereafter, the pH attains a steady value of  $\sim 9.1$ , reaching a maximum of 9.16 (for both the  
 408 top and bottom spent media) at 480 h, before finally dropping back to  $\sim 8.3$  at  $\sim 720$  h. This  
 409 implies that as cells grow, they actively modulate the pH of their environment. Across all  
 410 measurements, the pH associated with the bottom sub-population was found to be higher than  
 411 that of the top sub-population (Fig. 4B), indicating the difference in local chemo-environment  
 412 experienced by the cells. Comparable changes in local pH have been reported previously for  
 413 native algal cultures [37, 38], while small variations in exogenous stressor concentrations,  
 414 e.g., via  $H_2O_2$  or altering the carbonate chemistry (which also induce change of local pH)  
 415 could be sufficient to impact the swimming characteristics of *H. akashiwo* [13, 39].

416



417

418 **Fig. 4. Variation of the local pH tunes gravitactic swimming.** (A) Variation of the pH values (mean  
419  $\pm$  s.d.) over time, for the spent media obtained from the top and bottom sub-populations.  $t = 0$  h  
420 corresponds to the measurement done immediately after inoculation. The pH of the pure medium is  
421 indicated by the arrow. Measurements are done on two biological replicates ( $n = 2$ ), with multiple  
422 technical replicates in each case. (B) Difference of pH of the spent media (bottom minus top),  
423 corresponding to the above time points. (C)-(F) To capture the effect of the filtrate pH on cell  
424 populations: four different combinations of cells and spent media were designed. Corresponding effects  
425 of the spent media on the cell morphology were measured, as described previously ( $N = 10$ ,  
426 representative single cell images are shown in panels (C)-(F) insets). (C) Represents top filtrate mixed  
427 with top subpopulation [filtrate, cell] = [T, T]. The bottom right inset shows  $c/a$  values, which change  
428 from  $0.11 \pm 0.06$  at  $t = 0$  min to  $0.03$  at  $t = 120$  min (at  $t = 20$  min and 60 min, the values are  $0.12 \pm$   
429  $0.02$  and  $0.05 \pm 0.02$  respectively). (D) [B, B]: Bottom filtrate mixed with bottom subpopulation results;  
430 the  $c/a$  value changes from  $0.08 \pm 0.04$  at  $t = 0$  min to  $0.01 \pm 0.02$  at  $t = 120$  min (at  $t = 20$  min and 60  
431 min, the values are  $0.11 \pm 0.05$  and  $0.05 \pm 0.04$  respectively). (E) [B, T]: Bottom filtrate mixed with the  
432 top subpopulation; The  $c/a$  value remains nearly constant between  $0.07 - 0.08$  ( $c/a = 0.08 \pm 0.04$ ;  $0.07$   
433  $\pm 0.05$ ;  $0.08 \pm 0.04$  and  $0.07 \pm 0.02$  at  $t = 0, 20, 60$  and  $120$  min). (F) [T, B]: Top filtrate mixed with  
434 bottom cells;  $c/a$  values are  $0.08 \pm 0.02, 0.06 \pm 0.02, 0.12 \pm 0.02$  and  $0.02 \pm 0.03$  at  $t = 0, 20, 60$  and  
435  $120$  min. The swimming stability shifts over time, from negative to positive gravitaxis, indicated by the  
436 arrow heads, for [B, B], [T, T] and [T, B] combinations (equivalent to the isolated top and bottom sub-  
437 populations, Fig. 3), while for the mixed case, [B, T], presence of the bottom filtrate enables the cells  
438 from the top subpopulation to maintain their morphology, thereby hindering any shift in the swimming  
439 stability.

440

441 To confirm the role of the local pH in driving the observed changes in cell morphology, and  
442 consequently, the swimming behavior, we exposed cells from each sub-population to their  
443 own (control) and to the complementary (test) spent media, thereby analyzing 4 different  
444 combinations: [spent media, cells] = [T, T], [B, B], [B, T] and [T, B], where T and B  
445 respectively denote Top and Bottom (Fig. 4C-F). The morphological data corresponding to  
446 the combinatorial experiments are presented in Figures S11-S15.

447 When cells from the top (bottom) sub-population were introduced with their own spent  
448 media, the fore-aft asymmetry,  $c/a$ , changed from  $0.12 \pm 0.06$  ( $0.08 \pm 0.05$  for bottom) at  $t =$   
449  $0$  min. to  $0.04 \pm 0.01$  ( $0.04 \pm 0.03$ ) at  $t = 120$  min (inset, Fig. 4C, D), resulting in comparable  
450 shifts in the swimming stability of each of the sub-populations as shown in Fig. 4 C, D for  
451 the [T, T] and [B, B] combinations respectively (for both cases, the swimming stability  
452 reduces, as also observed in Fig. 3H for the isolated sub-populations). Over similar  
453 timescales, the [T, B] combination showed similar response (Fig. 4 F and inset): the  $c/a$   
454 changed from  $0.08 \pm 0.03$  at  $t = 0$  min. to  $0.03 \pm 0.03$  at  $t = 120$  min; with an overall  
455 reduction of the swimming stability.

456 Exceptionally, the morphological alteration and the resulting changes in the swimming  
457 stability differs for the [B, T] combination, wherein cells from the top sub-population are  
458 introduced to the spent media from the bottom sub-population. In this case, no perceptible  
459 change in the cell asymmetry was observed over time (Fig. 4E and inset) with the  $c/a$   
460 maintaining a steady mean value between  $0.07$  and  $0.08$ . Alongside, the swimming stability  
461 remains positive throughout, indicating that the cells maintain an up-swimming behavior  
462 (against gravity) over the entire observation window, in contrast to the other three  
463 combinations. We attribute this distinct tendency of the top sub-population to remain further

464 away from the bottom filtrate to the relatively higher pH of the spent media associated with  
465 the bottom sub-population; thus rendering the bottom filtrate relatively more potent in  
466 triggering the vertical separation of the sub-populations in the cell culture, than the other way  
467 round. Overall, the combinatorial experiments suggest that the top and bottom sub-  
468 populations emerge due to the differential response of the *H. akashiwo* population, at  
469 individual scale, to the local pH. Despite difference between the absolute *c/a* values of the top  
470 and bottom sub-populations, cells show similar swimming behavior and temporal trend under  
471 isolated conditions, which however was altered by the introduction of the spent media. The  
472 alteration of the morphological and motility traits indicates that in presence of the  
473 complementary spent media, cells—with otherwise similar traits—can elicit distinct responses  
474 which highlight the role of chemo-regulation of the local environment in tuning the  
475 phenotypic traits actively, ultimately resulting in emergent spatial distribution of sub-  
476 populations within a growing cell culture.

477

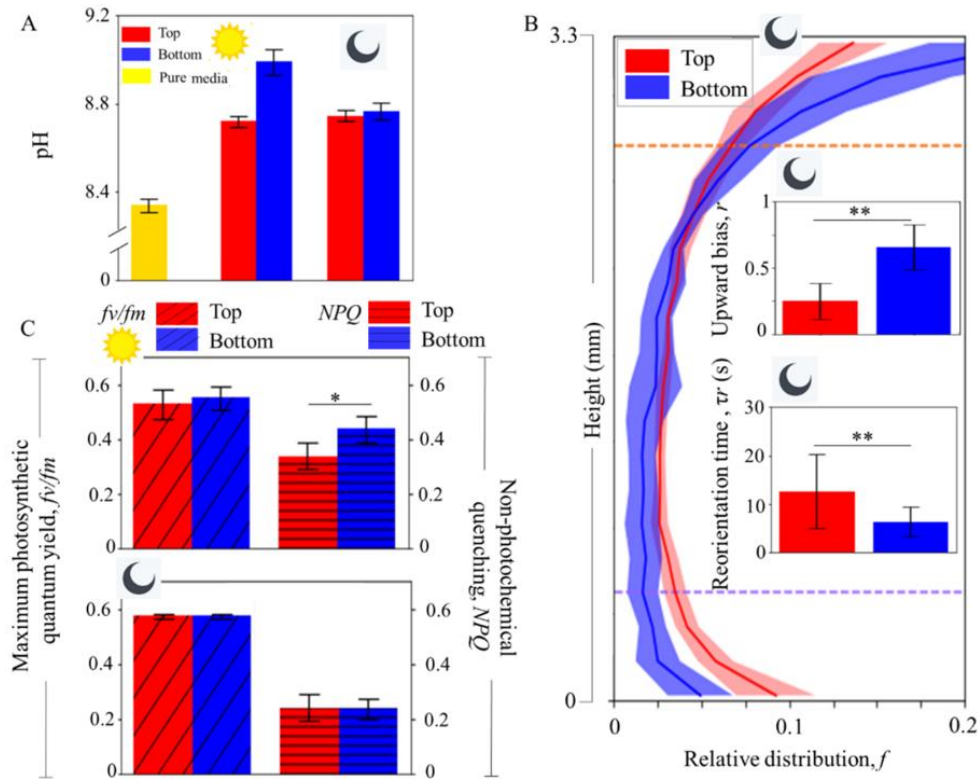
### 478 **Diel variation of the local pH, photophysiology and night-time swimming behavior**

479 In order to obtain insights throughout a 24 h cycle, we carry out night-time pH measurements  
480 on the spent media associated with the top and the bottom sub-populations of a 96 h culture  
481 (Materials and Methods). As shown in Fig. 5A (right most bars), the night-time difference in  
482 pH,  $\sim 0.02$  ( $8.96 \pm 0.04$  vs  $8.94 \pm 0.03$ ), is much lower than the day-time difference of the pH  
483  $\sim 0.37$  ( $9.09 \pm 0.06$  vs  $8.72 \pm 0.03$ ). While the pH of the top filtrate remains nearly constant,  
484 the pH of the bottom filtrate shows a considerable drop between the day and night-times.  
485 Alongside, at night-time, the bottom sub-population shows a significantly higher upward bias  
486 (Fig. 5B). The drop in the pH promotes downward swimming of the top sub-population,  
487 thereby aiding DVM following the circadian rhythm (Fig. 5B, upper inset). In contrast, the  
488 reduction of the reorientation timescale of the bottom sub-population (Fig. 5B lower inset,  
489 and Fig. S16), indicates that these cells are now primed to swim against gravity, thus  
490 confirming that the bottom sub-population possesses an out-of-phase circadian swimming  
491 behavior.

492

493 Under optimal conditions, DVM patterns—mediated by the internal circadian rhythm—allows  
494 phytoplankton species access to sunlight and nutrients while avoiding detrimental factors  
495 including predators. As such, an out-of-phase pattern would emerge when the fitness benefits  
496 are limited under evolutionarily established DVM. In our case, 96 h after the inoculation, the  
497 nutrient levels are considerably reduced, and will be fully depleted within  $\sim 200$  h. Thus, it  
498 could be advantageous for a population to expand its vertical distribution to enhance the  
499 search radius for resources, as well as spread over a larger space to grow and divide without  
500 crowding. This may be achieved through turning a part of the population to swim downwards  
501 (forming the bottom sub-population), as against all the cells competing for limited resources  
502 and space by swimming up (top cells). Such an active diversification of the swimming  
503 strategy could be further rationalized if, additionally, the emergent sub-populations possessed  
504 differential photophysiology and ability to alleviate light stress (top swimmers will be, on  
505 average exposed to higher doses of light than those at the bottom). By carrying out pulse-  
506 amplitude modulated chlorophyll fluorometry (PAM) assays on each of the sub-populations,  
507 we estimate their photophysiology during the day and night-times (Fig. 5C). While there is no  
508 statistically significant difference between the maximum photosynthetic quantum yield,  $f_v/f_m$ ,  
509 and the maximum electron transfer rate,  $ETR_{max}$  (Fig. S17) either during day or night, the  
510 NPQ values show a significant difference during the day-time and no difference at night time.

511 This indicates that the cells from the bottom sub-populations are at a higher oxidative stress  
 512 level than top ones (in agreement with observations from natural systems). This may explain  
 513 why the bottom cells are rounder (lower  $c/a$ ), and can also result in production of excess  
 514 extracellular ROS (e-ROS) by the bottom cells, thus rendering the bottom environment more  
 515 potent as an effective info-chemical as seen in Fig. 4. When either sample was isolated and  
 516 dark-adapted for 20 min., there was no notable difference in any of the photophysiological  
 517 parameters, indicating that, in absence of the complementary sub-population, the  
 518 photophysiological parameters are comparable as also seen for the other traits. Thus, we can  
 519 conclude that even though cell samples at top and bottom have similar photosynthetic  
 520 efficiency, the capacity of stress handling is different. So, it would be beneficial for some  
 521 cells to stay at top and others at bottom. One key feature of vertical sub-populations is the  
 522 fact that in isolation, they show effectively comparable behavior and physiology, and thus  
 523 present functionally equivalent states. In natural marine settings, this may be critical for  
 524 species survival especially if a portion of the population gets eliminated by deleterious  
 525 stimuli like turbulence, the other sub-population can effectively function and maintain the  
 526 biological fitness of the species.  
 527  
 528



529  
 530  
 531

532 **Fig. 5. Diel variation of local pH underpins night-time swimming behaviour of gravitactic sub-**  
 533 **populations.** (A) Night-time pH of the spent media obtained from the top and the bottom sub-  
 534 populations (20:00 h CEST, rightmost bars) 96 h after inoculation, as compared to the daytime values  
 535 (11:00 h CEST,  $n = 3$  in each case). The night-time difference in pH,  $\sim 0.02$  ( $8.96 \pm 0.04$  vs  $8.94 \pm 0.03$ ),  
 536 is much lower than the day-time difference of the pH  $\sim 0.37$  ( $9.09 \pm 0.06$  vs  $8.72 \pm 0.03$ ). The pH of the  
 537 bottom filtrate shows considerably higher drop (from day to night), while the pH of the top filtrate  
 538 remains nearly constant. (B) Vertical distribution of the top (red line and shaded region show  
 539 respectively the mean and s.d.,  $n = 6$ ,  $N = 1614 \pm 395$ ) and the bottom (blue line and shaded region,  $n =$   
 540  $6$ ,  $N = 1112 \pm 418$ ) sub-populations at night-time, around the midnight (00:00 h, indicated by a crescent  
 541 moon). The upper bar plot in the inset shows corresponding upward bias index ( $r$ ):  $0.26 \pm 0.14$  for top

542 and  $0.66 \pm 0.17$  for bottom, reveal significantly higher up-swimming stability of the bottom  
543 subpopulation at night-time ( $p < 0.05$ , two asterisks, 2 tailed t-test). The lower inset plotting the  
544 swimming stability in terms of the reorientation timescale,  $\tau_r$  (mean  $\pm$  s.d.):  $2.6 \pm 6$  s for the top ( $n = 12$ ,  
545  $N = 733 \pm 174$ ) and  $6.3 \pm 3$  s for the bottom ( $n = 12$ ,  $N = 545 \pm 207$ ) sub-populations. The timescales  
546 are significantly different,  $p < 0.05$  (two asterisks), verified using a 2 tailed t-test. (C) Top panel presents  
547 the daytime (marked with a sun) maximum photosynthetic quantum yield,  $f_v/f_m$  for the top (red,  $n = 4$ )  
548 and the bottom (blue,  $n = 3$ ) sub-populations after two minutes of dark adaptation. No statistically  
549 significant difference was noted ( $p = 0.63$ , 2 tailed t-test). However, the non-photochemical quenching  
550 ( $NPQ$ ) values show significant difference ( $p < 0.1$ , indicated by the asterisk on the bar plot on the right).  
551 In the bottom panel (night-time), the bar plots in the left show maximum photosynthetic quantum yield,  
552  $f_v/f_m$  for top (red,  $n = 2$ ) and bottom (blue,  $n = 2$ ) samples after two minutes of dark adaptation. No  
553 statistically significant difference is noted (2 tailed t-test,  $p = 0.94$ ), also for the corresponding  $NPQ$   
554 values ( $p = 0.96$ ).

555

## 556 Discussion

557 Recent studies suggest that the production of info-chemicals (signaling molecules) by  
558 phytoplankton can regulate population-scale behavior, offering potential biological functions  
559 like avoiding predators [40-42]. Studies show that change in the exogenous pH can trigger  
560 change in swimming behavior and potentially alter the DVM pattern of phytoplankton [39].  
561 Decrease in pH values from 8.26 to 8.13 was sufficient to induce increased downward  
562 swimming in *H. akashiwo*. In natural settings, pH variations occur due to the direct addition  
563 and removal of dissolved inorganic carbon (DIC) owing to photosynthesis and cellular  
564 respiration [43]. Over the course of a 24 h period, metabolic processes [44, 45], in  
565 combination with hydrodynamic factors [46, 47], can engender considerable changes in the  
566 local pH. Our results agree with reported observations on the impact of pH on the motility, a  
567 key difference that we note here is that the cells, as they grow, modulate their local pH to  
568 generate distinct sub-populations. The pH associated with the top and bottom sub-populations  
569 represent considerable difference in the local alkalinity experienced by the cells, resulting in  
570 distinct behavioral responses when cells are introduced to their complementary spent media  
571 (as revealed by the combinatorial experiments). This ultimately leads to the vertical  
572 separation of the sub-populations within a growing culture, with the relative difference in the  
573 local pH acting as an effective info-chemical.

574 An alternative relevant mode of cell-to-cell chemical communication is the quorum sensing,  
575 wherein signalling molecules called autoinducers are released when local population density  
576 reaches a critical value, particularly under confinements [48, 49]. So as to ascertain if the  
577 phytoplankton traits observed here emerges due to quorum sensing, we studied cells from  
578 continuous cultures at 48 h and 96 h of after inoculation (Fig. S18). At 48 h, the upward bias  
579 (mean  $\pm$  s.d.) is  $0.52 \pm 0.27$  for the top cells, and  $0.48 \pm 0.21$  for the bottom cells. We note  
580 that in isolation, the top and the bottom cells showed similar upward bias values as for the  
581 cells which were in the 96 h culture (data shown in Fig.1). The 48 h culture had a higher  
582 upward bias than the 96 h population, indicating that younger cell cultures comprised higher  
583 proportion of up-swimming cells, in agreement with the DVM trends generally observed. As  
584 shown in Fig. 1A, B, the emergent sub-populations are observed around 96 h, when the  
585 population density is  $\sim 3$ -fold relative to that at 48 h. If a quorum-like behavior triggered the  
586 emergence of sub-populations in cultures older than 48 h, diluting 96 h culture (to match the  
587 cell concentration at 48 h) should drive the upward bias values higher. However, no such  
588 enhancement of the upward bias values in the diluted 96 h cell cultures were observed (Fig.

589 S18), confirming that the sub-populations emerge due to co-existence, and not by a high  
590 population density of the cells. The lack of a quorum-like behavior is further confirmed when  
591 we expose the sub-populations to their corresponding (or complementary) spent media as  
592 discussed in Fig. 4. This conclusively indicates that it is cue for the emergent behavior lies in  
593 the spent media, effectively acting as an info-chemical that diversifies the circadian  
594 swimming behavior.

595 Finally, we tested an additional mode of communication commonly found in phytoplankton  
596 communities: extracellular vesicles (EVs). EVs have been shown to mediate cell-cell  
597 communications over large distances [50]. While we detected low concentrations (~10-  
598 100/ml) in our experiments, careful investigation of our samples did not however yield any  
599 observable differences in the circadian swimming behavior when we compared swimming  
600 behavior in the presence or the absence of the EVs in the local environment.

601 In conclusion, we have shown that a monoclonal phytoplankton population can engender  
602 behaviorally distinct phenotypes over time, due to *in situ* variation of the local pH. The  
603 emergent phenotypes are behaviorally plastic, and can play interchangeable functional roles  
604 depending on the time of the day (light vs dark periods). Although both subpopulations were  
605 found to be negatively gravitactic during daytime, one performed better than the other under  
606 co-existing conditions, thus leading to a vertical segregation of the population into strong and  
607 weak up-swimmers. Evolutionarily, cells are programmed to be up-swimmers during daytime  
608 (to get light for photosynthesis), so, those which do not show strong up-swimming behavior  
609 may compromise fitness. To circumvent this potential drop in fitness, the sub-populations  
610 develop complementary circadian swimming patterns, additionally enabling the population,  
611 as a whole, to expand their vertical niche which is advantageous for accessing resources as  
612 well as increasing the survival probability. While at a population scale, circadian swimming  
613 is harnessed to make the system robust and dynamic, at a single cell level, cells leverage  
614 environmental pH as a intra-population communication cue to trigger their vertical  
615 segregation. As the overall pH of the medium becomes basic, cells which are strong up-  
616 swimmers, are capable of reducing the pH of local environment (acidic) during day and vice  
617 versa. This in turn, reduces (pH) stress, making them more fore-aft asymmetric and better up-  
618 swimmers. Change in morphology due to stress may be associated with the production of  
619 reactive oxygen species (ROS) in *H. akashiwo* [7, 13]. Phytoplankton are major producers of  
620 ROS in marine environments and many species are known to produce e-ROS even under  
621 optimal growth conditions [51]. Production of extracellular ROS can be a possible  
622 mechanism to get rid of excess endogenous or surface ROS [52, 53]. While e-ROS has been  
623 attributed to functions like predator avoidance, resistance to viral infection, and toxicity in  
624 case of HABs, they have also been associated to allelopathic interactions and communication  
625 with other species [40]. Thus, ROS, alongside reactive nitrogen species [42], can potentially  
626 act as cues for conspecific cell-cell communication and signaling. Based on their chemical  
627 forms, reactive species have the potential to alter the pH of the local media, and therefore,  
628 may be at play in mediating the emergent phytoplankton behavior we have reported here. In  
629 marine ecosystems, changes in the pH depend on the buffer capacity of the seawater, which,  
630 due to ongoing anthropogenic stresses is expected to decline in the future. This may have  
631 profound implications for food webs: not only photosynthesis of phytoplankton, but also  
632 swimming and hence photosynthetic efficiency of motile species will be directly impacted.  
633 Globally, as the ocean waters see a rapid change in the pH [54], our results will provide a



634 mechanistic basis for assessing the impacts of ocean acidification on phytoplankton  
635 migratory patterns, and shed light on the transport, fitness and adaptation of phytoplankton  
636 inhabiting oceans of the future.

637

638

## 639 **MATERIALS AND METHODS**

### 640 **Cell Culture**

641 Cells were cultured in 50-ml sterile glass tubes with 14:10 hours of light and darkness (to  
642 simulate a diel cycle) in f/2-Si (minus silica) medium at 22°C and constant light intensity (of  
643 1.35mW, during light phase). They were propagated every 1 to 2 weeks, by inoculating 2 ml  
644 of cell suspension collected from ~0.5 mm of the top of a parent culture (mother culture), into  
645 25 ml of fresh medium, in a laminar flow chamber. White light (wavelength,  $\lambda=535$  nm,  
646 power =1.35 mW) illuminates the incubator between 4 hours to the end of 17 hours (yellow  
647 line) and mimics daytime. It is switched off automatically at the start of 18<sup>th</sup> hour till the 4<sup>th</sup>  
648 hour of the next day (gray line), to represent night. Experiments are usually performed  
649 between 11 to 15 hours, indicated by the green line region. For all experiments reported in  
650 this paper, we used cultures that were 96 hours old (early exponential phase of growth). All  
651 daytime experiments were conducted between 10 hours to 16 hours to rule out any DVM  
652 related impact. Nighttime experiments were conducted between 20 hours to 22 hours. We  
653 started 24-hour experiments at 11 hours of one day and concluded at the same time of the  
654 next day. For each study, unless mentioned otherwise, we used at least four replicates, the  
655 details of which are provided in their corresponding sections. All experiments reported here  
656 can be broadly classified into a) population scale and b) single-cell level. The experimental  
657 setup and protocol for both categories are outlined below. Unless otherwise mentioned, all  
658 experiments reported in this article uses cells that are about 96 h old. For all experiments  
659 reported in this article, cells are collected from  $\pm 5$  mm of the 2 different regions shown on  
660 the culture tube. Cells collected from the red box indicated region of the culture tube are  
661 ‘Top’ samples and the blue box corresponds to ‘Bottom’ samples.

662

### 663 **Quantification of growth curve**

664 To quantify growth curve, fresh cultures were prepared from parent cultures. Cells were  
665 allowed to grow for 24 hours from whence, measurements were taken. For the 0-hour time  
666 point reading, cells were collected from the parents separately and counted. The count was  
667 then normalized assuming dilution in a 25 ml culture and from this the final count was taken.  
668 From 24 hours, cells in the cultures were counted in a 3.5  $\mu$ l chamber and observed under a  
669 stereo microscope (Nikon ® SMZ1270). Readings were taken for 24, 48, 72, 96, 192, 264,  
670 336, 384, 432, 552 and 672 hours (28 days). The counts were converted to the appropriate  
671 units and growth curve was plotted (count as a function of time). To calculate doubling time  
672 from this data, cell count was replotted in log scale against time. The time points showing  
673 linear curve (indicative of exponential growth/ doubling growth) i.e., 0 to 96 h were selected.  
674 From this, growth curve was calculated as

675 
$$r = (\ln \frac{C_f}{C_i}) / (t_f - t_i)$$

676 where  $r$  is the growth rate,  $C_f$  and  $C_i$  are cell concentrations between consecutive time points  $t_f$   
677 and  $t_i$  (e.g. 24 and 0 h, 48 and 24 h, and so on). From this, doubling time was calculated as

678 
$$dtm = \frac{\log 2}{r}$$

679 where  $dtm$  is the doubling time. The  $dtm$  of each pair of timepoints were averaged to obtain  
680 the mean ( $\pm$  s.d.), which is reported.

681

## 682 **Cell harvesting and preparing cell filtrate**

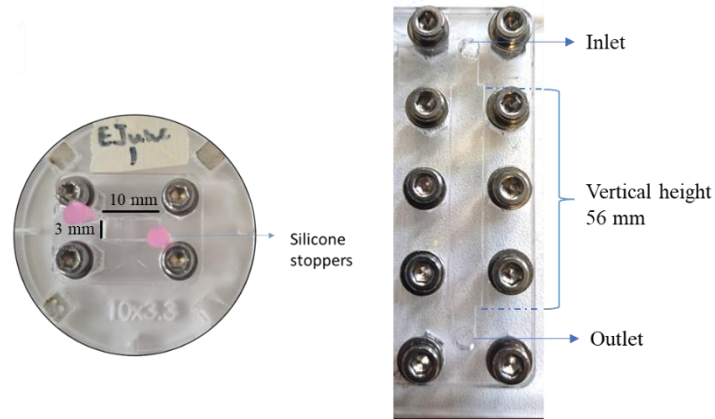
683 For each experiment reported, unless otherwise mentioned, two types of samples were used:  
684 top samples: which are cells collected from the approximately the first 0.5 mm of the culture  
685 using 1ml pipette (+tips) and bottom samples, which are cells collected from around 0.7 mm  
686 above the base of the culture tube. To collect this, Sterican<sup>®</sup> disposable long needles (120 mm  
687 x 0.8 m) were used with Injekt<sup>®</sup> disposable syringes. This harvesting involves collection of  
688 cells plus their surrounding fluid medium. In experiments where just the medium was needed,  
689 cells were filtered out using 1 $\mu$ m (pore size) Whatman<sup>®</sup> Puradisc 25 syringe filter. The  
690 detailed steps are shown visually in supplementary Fig. S2.

691

## 692 **Population scale experiment**

### 693 **i) Quantification of vertical distribution from an equilibrium state**

694 All vertical distributions were observed in either a ‘small’ (10 mm x 3.3 mm x 2 mm) or a  
695 ‘tall’ (60 mm x 3.3 mm x 2 mm) chamber made of polymethyl methacrylate. For small  
696 chamber experiments, a chamber was mounted on a custom cage for visualization and imaged  
697 using a lens-camera setup. The cage is equipped with  $xz$  translation screws, with a maximum  
698 displacement of 25 mm. The entire setup, as well the calculation methodology is detailed in  
699 [14]. Cells were filled into it and visualized at  $\sim 1.7$  x zoom, using a Grasshopper3 (model:  
700 GS3-U3-41C6C-C) camera with an 1" sensor. At this zoom, the entire chamber was captured  
701 in one go. The chamber was illuminated with a red LED (630 nm wavelength). Imaging was  
702 done in the middle region (horizontal) of the chamber to stay away from the inlets and  
703 boundary walls. After filling, cells were allowed 20 minutes to reach their steady distribution  
704 which was then imaged.



705

Small Chamber

Tall Chamber

706 For the tall chamber experiments, a chamber of height 60 mm (shown below) was mounted  
707 on a stage which was made by coupling two  $xz$  translation stages in a series, allowing an  
708 increased displacement span of at least 55 mm along the vertical. Cells were filled and  
709 allowed 20 minutes to reach a steady distribution (called pre-flip distribution). At  $\sim 1.4 \times$   
710 zoom, our camera could capture  $\sim 4$ mm per frame, so we had to move our chamber about 14  
711 times for the camera to capture the entire 56 mm. We excluded the top and bottom 4 mm of  
712 our chamber as these regions are close to the inlet and outlet ports and i) imaging is not clear  
713 due to projection of stopper (used for sealing the ports) on the imaging plane and ii) avoid  
714 any bias arising due to any potential air-medium interface at the ports. For the remaining 56  
715 mm, we stitched the regions together and obtained the complete distribution of the chamber  
716 and used for downstream calculations. Scanning the entire chamber (14 regions) took  $\sim 2$   
717 minutes, which is less than time taken by cells to cover a region.

718

### 719 **ii) Computing upward bias index**

720 To quantify the upward bias, we used the equation  $r = (f_{\uparrow} - f_{\downarrow}) / (f_{\uparrow} + f_{\downarrow})$ , where  $f_{\uparrow}$  and  $f_{\downarrow}$  are  
721 the concentration of cells in the top and bottom 660  $\mu\text{m}$  of the chamber, respectively. The  $r$   
722 value lies between -1 to 1. An upward bias value of  $\sim -1$  means all cells are present in the  
723 bottom portion of the chamber, while a value of  $\sim +1$  means all cells at top. An upward bias  
724 value of 0 means a 50:50 distribution of cells between the top and bottom regions.

725

### 726 **iii) Computation of motility parameters from single cell tracking**

727 Cells were put in the small chamber as described above and allowed 20 min. to reach a steady  
728 distribution as mentioned above. Then the chamber was rotated by 180 degrees (in 3 seconds)  
729 via an Arduino controlled automatic stepper motor (programmed in-house). As the cells  
730 started to swim back to their steady state, short videos of about 160 frames @ 16fps (frames  
731 per second) were captured. Starting from the first second of swimming (16<sup>th</sup> frame), 120  
732 frames were chosen, corresponding to 7.5 seconds of swimming. Individual cell coordinates  
733 were determined via binarizing and thresholding using the OpenCV2 module in python. Cell  
734 coordinates were linked for subsequent frames via the Trackpy module, to obtain a list of all  
735 trajectories. From this, speed, horizontal component, and vertical component of swimming

736 velocity was computed. To ensure selection of the best trajectories, a) all tracks shorter than  
737 45 frames and b) tracks with displacement less than  $\sim 2 \mu\text{m}$  ( $1/10^{\text{th}}$  of a cell body length) and  
738 c) speeds  $< 10 \mu\text{m}/\text{sec}$  or  $> 200 \mu\text{m}/\text{sec}$  were rejected.

739

#### 740 **iv) Computing cell stability from reorientation**

741 Cell steady distribution was reached, and the small chamber was rotated as described above.  
742 As the cells reached the middle of the chamber, 3 180-degree flips were applied (with waiting  
743 times of 15, 12, and 12 seconds). Out of this, data from the 1<sup>st</sup> and 2<sup>nd</sup> flips were used for  
744 analysis. Each of these data is termed a ‘sub-replicate (SR)’. Videos were acquired at 16 fps  
745 and cells were tracked as described above. 160 corresponding to 10 sec of swimming were  
746 sufficient to capture multiple cell reorientation events in each flip. Trajectories less than 45  
747 frames or a net displacement  $< 20 \mu\text{m}$  were filtered out. The remaining trajectories were  
748 interpolated quadratically (smoothing). For the single trajectory, angular velocity ( $\omega$ ) was  
749 obtained for each consecutive frame as a function of the instantaneous angular position ( $\theta$ ).  
750 Angular velocities were averaged for a given  $\theta$  value (ranging from  $-180^\circ$  to  $180^\circ$ , binned at  
751 intervals of  $30^\circ$ ). Any  $\omega$  value greater than  $0.5 \text{ rads}/\text{sec}$  or less than  $-0.5 \text{ rads}/\text{sec}$  was  
752 eliminated. Obtained  $\omega$  values were fitted to a sinusoidal curve of the form  $A \times \sin(x)$ , and the  
753 reorientation time scale ( $\tau_r$ ) was then obtained as  $\tau_r = \frac{1}{2A}$ .

754

#### 755 **v) Measuring the nutrient concentrations**

756 Concentration of two primary nutrients pertaining to phytoplankton growth, nitrate ( $\text{NO}_3^-$ )  
757 and phosphate ( $\text{PO}_4^{3-}$ ), were measured through photometry using Prove600 Spectroquant  
758 (Merck) spectrophotometer. For this, cell filtrate was collected from top and bottom of the  
759 culture.  $\text{NO}_3^-$  concentration was analyzed with Nitrate Cell Test in Seawater (method:  
760 photometric 0.4 to 13.3 mg/liter  $\text{NO}_3^-$  Spectroquant) with a minimum detection limit of 6.45  
761  $\mu\text{M}$ .  $\text{PO}_4^{3-}$  concentration was analyzed with phosphate cell test (method: photometric 0.2 to  
762 15.3 mg/liter  $\text{PO}_4^{3-}$  Spectroquant) with a minimum detection limit of 2  $\mu\text{M}$ ). Below this limit,  
763 values below the respective detection limits are taken as zero.

764

#### 765 **vi) Measuring photophysiology using Pulse-amplitude modulated (PAM) chlorophyll** 766 **fluorometry**

767 A Multiple Excitation Wavelength Chlorophyll Fluorometer (Multi-Color-PAM; Heinz Walz  
768 GmbH, Effeltrich, Germany) was used to quantify the maximum photosynthetic quantum  
769 yield ( $F_v/F_m$ ), the maximum electron transport rate ( $ETR_{\text{max}}$ ), and non-photochemical  
770 quenching ( $NPQ$ ) of a cell suspension. For measurements, 1.2 ml cell suspensions were  
771 placed into a quartz-silica cuvette (Hellma absorption cuvettes; spectral range, 200-2500 nm;  
772 pathlength, 10 mm). PAMWin software saturation pulse (SP) and light curve methods were  
773 used to quantify  $F_v/F_m$ ,  $ETR_{\text{max}}$  and  $NPQ$  per experiment. The samples were dark adapted  
774 (DA) for  $< 1 \text{ min}$ . before measurement. Literature suggests that PAM samples should have a  
775 DA time of at least 15 min to remove any pre-stress/ difference in samples due to different  
776 light/growth conditions present in samples that can bias the measurements. However, i) our

777 samples are all grown and maintained under same conditions and if there is any difference in  
778 stress levels, it is possibly due to difference in physiology or other factors between the  
779 subpopulations and ii) in our case we are interested to measure the ‘native states’ of the  
780 samples i.e. how they are in the culture itself and the longer waiting time, the more identical  
781 they start to become. This is also seen in our experiments with *DA* of 20 min. (data not  
782 shown), which indicates that in coexistence, the stress levels (*NPQ*) are different than in  
783 isolation, similar to swimming behaviors of isolated vs mixed samples.

784

## 785 **vii) Measuring pH of the spent media**


786 For measuring pH of medium/samples, ~3ml pure medium (kept in incubator under same  
787 condition as cells)/ spent media were collected into a 15ml plastic falcon tube. Into this, the  
788 electrode of a Mettler Toledo FiveEasy Plus (FP20) Benchtop pH/mV Meter (post-calibration  
789 with buffers of pH 4.01, 7.0 and 9.21) was inserted and pH values were obtained.

790

**Table 1.** pH of the samples measured in experiments.



Time point (h)	Top	Bottom
0	8.34 ± .05	8.36 ± .05
48	8.72 ± .03	8.82 ± .04
96	9.01 ± 0.023	9.09 ± 0.06
144	9.09 ± .04	9.18 ± .05
240	9.09 ± 0	9.12 ± .01
432	9.16	9.16
720	8.26 ± .03	8.27 ± .05
		797
		198
		96
	8.94 ± 0.03	8.96 ± 0.04



799

## 800 **Single cell experiment**

### 801 **i) Computing fore-aft asymmetry parameters from cellular morphology**

802 To observe morphology as a function of time, 500 µl cells were pipetted out from a culture  
803 tube and put into 1.5 ml glass vials. This was covered with a parafilm and perforated with a  
804 single needle and stored in the same incubator as the culture tube (22° C). 10 µl cells were  
805 pipetted out at 0 (immediately after cells were collected from the culture tube), 20, 60 and  
806 120 min. These were put on a glass slide and covered with a coverslip and put under a  
807 microscope (Olympus CKX53 inverted) and viewed in phase contrast mode using a camera  
808 (same as above). Short videos of cells were captured at 82 fps and at least 10 cells were  
809 imaged per time point.

810 To analyze morphology, a single frame showing a cell in maximum focus was chosen from a  
811 video manually. This was then cropped around the cell and using OpenCv2 module, points  
812 were drawn along the cell’s external contour and the *xy* coordinates per point were generated.

813 These were converted to polar co-ordinates and fit to a three-parameter 3D spheroid surface  
814 [55] which, in 2D, translates to:

815 
$$r = \frac{ab}{\sqrt{b^2 \cos^2 \psi + a^2 \sin^2 \psi}} + c \sin \psi$$

816 i.e., an ellipsoid with  $a$  and  $b$  as major, minor semi-axis [7]. This ellipsoid is fore-aft  
817 asymmetric i.e., in the direction of the major axis and this asymmetry is captured by the  
818 parameter  $c$ .

819

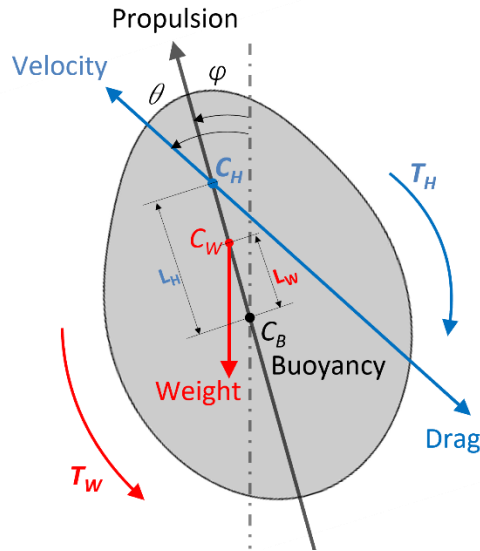
## 820 **ii) Computing fore-aft (a)symmetry parameters from cellular morphology in presence** 821 **of the spent media**

822 1.4 ml cell suspension of one type (top or bottom) was collected and 800  $\mu$ l of this  
823 suspension were put into two 1.5 ml glass vials (400  $\mu$ l each). The rest was filtered using a 1  
824  $\mu$ m Whatman<sup>®</sup> Puradisc 25 syringe filter, to form the filtrate (as described previously) of the  
825 same type. Next, 1ml of the other cell type was collected immediately and passed through the  
826 filter to form the opposite supernatant. 150  $\mu$ l of both supernatants were collected  
827 individually and put into one of the vials to form a total of two experimental cases per sample  
828 type. For each experiment, 10 cells were imaged under the same microscope as above, at least  
829 at 50 fps and analyzed using the same protocol as described above.

830

## 831 **iii) Cell mechanics model and calculation of the stability diagrams**

832 To determine the propensity of the cells to maintain their swimming stability (and their inherent  
833 cell reorientation timescale) under diverse condition, we employ a cell-level mechanistic  
834 formulation. The model takes into account the various forces and torques a phytoplankton cell  
835 experiences by virtue of its motion and cytoplasmic organelle (nucleus) position. Our primary  
836 aim is to identify the dominant forces and torques a motile cell encounter and establish the  
837 factors that determine their up-swimming stability. A cell generates a propulsive force,  $\mathbf{P}$   
838 (because of its flagellar dynamics) to maintain its active motion. The weight of the cell (due to  
839 combined influence of the nucleus, lipids and cytoplasm) and the upthrust (attributed to the  
840 finite cellular volume) on the cell are inherent forces owing to its physiological configuration.  
841 In addition, the cell motion induces a drag force attributed to the cell geometry and viscous  
842 effects. Torques on the cell structure is estimated about its centroid (or center of buoyancy,  $C_B$ ,  
843 see Fig. 6 below). The torque contributions on the cell mechanics are the following: torque due  
844 to nucleus and lipids (when their center of residence is not on  $C_B$ ), torque originating from  
845 viscous drag (in case of asymmetric cellular geometry), and resistive (viscous) torque due to  
846 cell rotation (with rotation speed  $\omega$ ). With the above physical considerations, we balance the  
847 forces and torques in each component to formulate the reduced-order model that reads (see Fig.  
848 6):  
849



850  
851 **Fig. 6.** Schematic of the cell geometry showing the forces and torques (about the center of buoyancy,  
852  $C_B$ ) acting on a phytoplankton cell.  
853  
854

$$P \sin \varphi = D \sin \theta$$

$$P \cos \varphi - D \cos \theta = (\rho_{cell} - \rho_{fluid}) V g = (\rho_{cyt} - \rho_{fluid}) V_C g + (\rho_N - \rho_{cyt}) V_N g \quad (1)$$

$$D \sin(\theta - \varphi) L_H - W_N \sin(\varphi_N) L_N = \underbrace{D \sin(\theta - \varphi) L_H}_{T_H} - \underbrace{W_N \sin(\varphi) L_W}_{T_W} = R \eta \omega$$

855  
856 The symbols  $\rho$ ,  $V$ ,  $W$ ,  $\eta$  and  $L$  denotes the density, volume, weight, medium viscosity, and  
857 distance from cell centroid respectively. Some of the symbols carry the subscripts *cyt*, *fluid*,  $C$ ,  
858  $H$ , and  $N$  which, respectively, refers to the cytoplasm, background medium (within which the  
859 cell remains submerged), the hydrodynamic center of the cell, and the cell nucleus.  $\varphi$  is the  
860 angle between the line of action of the propulsive force,  $\mathbf{P}$  (attributed to the resultant flagellar  
861 motion) and the line of action of gravity. Here  $\varphi$  and  $\mathbf{P}$  are unknowns, which needs to be  
862 determined as part of the solution. In reality, the motion of the cell does not follow the line of  
863 action of  $\mathbf{P}$ , hence an angular offset  $\theta$  (an experimentally observable parameter) with the  
864 vertical is assumed along which the cell moves.  $\varphi_N$  is the angle between the direction of  
865 gravity (vertical line) and the line joining  $C_N$  and  $C_B$  (note  $\varphi = \varphi_N$ , since we assume the center  
866 of gravity of the nucleus to lie on the major axis).  $D$  denotes the drag force whose knowledge  
867 requires the detail of the cellular geometry and its interaction to the surrounding fluid, the  
868 details of which are provided below.

869  
870 We describe the axisymmetric cell geometry with the generic equation

$$871 \quad r = \frac{ab}{\sqrt{(b^2 \cos^2 \gamma + a^2 \sin^2 \gamma) \cos^2 \psi + a^2 b^2 \sin^2 \psi}} + c \sin \psi$$

872  $(-\pi/2 < \psi < \pi/2)$ , and  $\gamma$  ( $0 < \gamma < 2\pi$ ) represents the major axis length, minor axis length  
873 (equal to the semi-major axis length), polar angle, and azimuth angle, respectively. Here  $c$   
874 implies the deviation from the symmetric shape along the major axis (fore-aft direction) and  $r$

875 denotes the position vector of the points on the cell surface (from the origin) as a function of  
876 the polar and azimuth angles.

877 The fore-aft asymmetry (value of  $c$ ) is quantified using the phase-contrast microscopy images  
878 of the cells whose contours are fitted with Equation 1 and  $\gamma = 0$ , resulting in the form

879 
$$r = \frac{ab}{\sqrt{b^2 \cos^2 \psi + a^2 \sin^2 \psi}} + c \sin \psi.$$
 Note that for a symmetric cell geometry ( $c = 0$ ), the

880 hydrodynamic center ( $C_H$ ) falls on the cell centroid ( $C_B$ ), and  $L_H$  vanishes. With the  
881 consideration that the cell shape may be assumed as a prolate spheroid, the drag of a symmetric  
882 prolate ellipsoid is expressed as  $D_{p,\perp} = 6\pi\eta r_{eq} U K_{p,\perp}$  where  $U$  and  $K$  are the translational velocity

883 and the shape factor, respectively, while  $P^{(\perp)}$  denotes the parallel (perpendicular) direction  
884 with respect to the major axis. The shape factors have the form

885 
$$K_p = \frac{4(t^2 - 1)^{3/2}}{3t^{1/3} \left\{ (2t^2 - 1) \ln \left[ t + (t^2 - 1)^{1/2} \right] - t(t^2 - 1)^{1/2} \right\}}$$
 and 
$$K_{\perp} = \frac{8(t^2 - 1)^{3/2}}{3t^{1/3} \left\{ (2t^2 - 3) \ln \left[ t + (t^2 - 1)^{1/2} \right] + t(t^2 - 1)^{1/2} \right\}}$$
 for

886 prolate spheroids [56, 57] where  $t = a/b$ . The net drag on the cell is dictated by its orientation  
887 and is given by  $D = D_p \cos(\alpha) + D_{\perp} \sin(\alpha)$  ( $D_p$  and  $D_{\perp}$  are the drag forces parallel and  
888 perpendicular to the major axis of the cell shape, respectively, and  $\alpha = \theta - \varphi$ ).

889  $R$  represent the coefficient of hydrodynamic rotational resistance and has the form

890 
$$R = C_R \frac{2(t^2 + 1)(t^2 - 1)^{3/2}}{3t \left\{ (2t^2 - 1) \ln \left[ t + (t^2 - 1)^{1/2} \right] - t(t^2 - 1)^{1/2} \right\}}$$
 [56] where  $C_R = 8\pi r_{eq}^3$ . With  $R$  defined, the

891 viscous torque on a prolate spheroid is estimated using  $\tau = R\eta\omega$  where  $\omega$  is the angular rotation  
892 rate (rad/s). Our aim is to obtain the angular rotation rate  $\omega$  from the above set of three coupled  
893 equations (Equation 1). Using the experimentally known values (Table 2) we draw a stability  
894 phase-plot that presents the value of the angular rotation rate as a function of shape asymmetry  
895 and cell geometry (estimated by varying  $L_H/a$  and  $L_W/a$ ). The stability phase plots demarcate  
896 the regions of stable up-swimmers from stable down-swimmers, thereby encompassing the  
897 various stability conditions of cell motility as a function of various environmental factors. Here  
898 we note that since the nucleus resides above the cell centroid, the effects of the lipids on the  
899 cell stability may be safely ignored.

900

901 **Table 2.** Parameters used to draw the phase-plot diagram for the cell stability.

Parameter Name (Symbol)	Value	Unit
Major radius ( $a$ )	7.5	$\mu\text{m}$
Minor radius ( $b$ )	4.9	$\mu\text{m}$
Fore-aft asymmetry	1.04	$\mu\text{m}$
Velocity ( $U$ )	150	$\mu\text{m/s}$
Velocity angle ( $\theta$ )	$\pi/6$	rad
Medium viscosity ( $\eta$ )	$10^{-3}$	Pa-s
Density of nucleus ( $\rho_N$ )	1.3	g/cc
Density of cytoplasm ( $\rho_{\text{cyto}}$ )	1.05	g/cc
Density of medium ( $\rho_{\text{fluid}}$ )	1.036	g/cc
Nucleus radius ( $r_N$ )	1.94	$\mu\text{m}$
Nucleus offset along major axis ( $L_N$ )	0.37	$\mu\text{m}$



902 **References**

- 903 **1.** R. W. Eppley, O. Holm-Harisen, J. D. H. Strickland, Some Observations on the Vertical  
904 Migration Of Dinoflagellates. *J Phycol.* **4**, 333–340 (1968).
- 905 **2.** J. J. Cullen, Diel vertical migration by dinoflagellates: roles of carbohydrate metabolism  
906 and behavioral flexibility. *Contr. Mar. Sci.* **27**, 135-152 (1985).
- 907 **3.** K. Kohata and M. Watanabe, Synchronous division and the pattern of diel vertical  
908 migration of *Heterosigma akashiwo* (Hada) Hada (Raphidophyceae) in a laboratory culture  
909 tank. *J. Exp. Mar. Biol. Ecol.* **100**, 209-224, (1986).
- 910 **4.** R. Margalef, Life-forms of phytoplankton as survival alternatives in an unstable  
911 environment. *Oceanologica Acta.* **1**, 493–509 (1978).
- 912 **5.** P. M. Glibert, Margalef revisited: A new phytoplankton mandala incorporating twelve  
913 dimensions, including nutritional physiology. *Harmful Algae* **55**, 25–30 (2016).
- 914 **6.** E. Litchman, C. A. Klausmeier, Competition of Phytoplankton under Fluctuating Light.  
915 *The American Naturalist* **157**, 170-187 (2001).
- 916 **7.** A. Sengupta, F. Carrara, R. Stocker, Phytoplankton can actively diversify their migration  
917 strategy in response to turbulent cues. *Nature* **543**, 555–558 (2017).
- 918 **8.** A. Sengupta, Microbial Active Matter: A Topological Framework. *Fron. Phys.* **8**, 184  
919 (2020).
- 920 **9.** E. L. Harvey, S. Menden-Deuer, T.A. Ryneerson, Persistent intra-specific variation in  
921 genetic and behavioral traits in the raphidophyte, *Heterosigma akashiwo*. *Fron. Microbiol.* **6**,  
922 1277 (2015).
- 923 **10.** O.H. Hewitt and H.M. Shaikh, The rhythm of many: biological rhythms in the marine  
924 environment, from macro-scale planktonic ecosystems to micro-scale holobionts. *Fron. Mar.*  
925 *Sci.* **8**, 744169 (2021).
- 926 **11.** D.K. Ralston, D.J. McGillicuddy Jr and D.W. Townsend, Asynchronous vertical  
927 migration and bimodal distribution of motile phytoplankton. *J. Plankton Res.* **29**, 803-821  
928 (2007).
- 929 **12.** A.K. Yamazaki and D. Kamykowski, A dinoflagellate adaptive behavior model: response  
930 to internal biochemical cues. *Ecological Modelling* **134**, 59-72 (2000).
- 931 **13.** F. Carrara, A. Sengupta, L. Behrendt, A. Vardi, R. Stocker, Bistability in oxidative stress  
932 response determines the migration behavior of phytoplankton in turbulence. *Proc Natl Acad*  
933 *Sci U S A.* **118**, e2005944118 (2021).
- 934 **14.** A. Sengupta, J. Dhar, F. Danza, A. Ghoshal, S. Müller, N. Kakavand, Active  
935 reconfiguration of cytoplasmic lipid droplets governs migration of nutrient-limited  
936 phytoplankton. *Sci Adv.* **8**, eabn6005 (2022).
- 937 **15.** J. J. Cullen, J. G. MacIntyre, Behavior, physiology and the niche of depth-regulating  
938 phytoplankton. *Nato Asi Series G Ecological Sciences* **41**, 559-580 (1998).

- 939 **16.** D. Kamykowski, Trajectories of Autotrophic Marine Dinoflagellates. *J. Phycol.* **31**, 200–  
940 208 (1995).
- 941 **17.** A. Sournia, Circadian periodicities in natural populations of marine phytoplankton. In  
942 *Advances in marine biology* **12**, 325-389, Academic Press (1975).
- 943 **18.** H. Van Haren, T. J. Compton, Diel Vertical Migration in Deep Sea Plankton Is Finely  
944 Tuned to Latitudinal and Seasonal Day Length. *PLoS One* **8**, e64435 (2013).
- 945 **19.** V. G. Bruce, The biological clock in *Chlamydomonas reinhardi*. *J Protozool.* **17**, 328–  
946 334 (1972).
- 947 **20.** D. Iliev, O. Voytsekh, E. M. Schmidt, M. Fiedler, A. Nykytenko, M. Mittag, A  
948 heteromeric RNA-binding protein is involved in maintaining acrophase and period of the  
949 circadian clock. *Plant Physiol.* **142**, 797–806 (2006).
- 950 **21.** K. I. Kucho, K. Okamoto, S. Tabata, H. Fukuzawa, M. Ishiura, Identification of novel  
951 clock-controlled genes by cDNA macroarray analysis in *Chlamydomonas reinhardtii*. *Plant*  
952 *Mol Biol.* **57**, 889–906 (2005).
- 953 **22.** S. Hwang, R. Kawazoe, D. L. Herrin, Transcription of *tufA* and other chloroplast-  
954 encoded genes is controlled by a circadian clock in *Chlamydomonas*. *Proc Natl Acad Sci U S*  
955 *A.* **93**, 996–1000 (1996).
- 956 **23.** T. Matsuo, K. Okamoto, K. Onai, Y. Niwa, K. Shimogawara, M. Ishiura, A systematic  
957 forward genetic analysis identified components of the *Chlamydomonas* circadian system.  
958 *Genes Dev.* **22**, 918–930 (2008).
- 959 **24.** D. Kamykowski, A. Yamazaki, Modeling Planktonic Behavior as a Complex Adaptive  
960 System. *Handbook of Scaling Methods in Aquatic Ecology*, 543–557 (2003).
- 961 **25.** D. Kamykowski, E. J. Milligan, R. E. Reed, Biochemical relationships with the  
962 orientation of the autotrophic dinoflagellate *Gymnodinium breve* under nutrient replete  
963 conditions. *Mar. Ecol. Prog. Ser.* **167**, 105–117 (1998).
- 964 **26.** D. Kamykowski, Sub-Thermocline Maximums of the Dinoflagellates *Gymnodinium*  
965 *simplex* (Lohmann) Kofoid and Swezy and *Gonyaulax polygramma* Stein. *Gulf of Mexico*  
966 *Science* **4**, (2018).
- 967 **27.** K. Wirtz and S.L. Smith, Vertical migration by bulk phytoplankton sustains biodiversity  
968 and nutrient input to the surface ocean. *Scientific Reports* **10**, 1142 (2020).
- 969 **28.** J.D. Wheeler, E. Secchi, R. Rusconi, R. Stocker, Not just going with the flow: The effects  
970 of fluid flow on bacteria and plankton. *Ann. Rev. Cell and Dev. Bio.* **35**, 213-237 (2019).
- 971 **29.** L. Legendre, S. Demers, C. Garside, E.M. Haugen *et al.*, Circadian photosynthetic  
972 activity of natural marine phytoplankton isolated in a tank. *J. Plankton Res.* **10**, 1-6 (1988).
- 973 **30.** A. Engesmo, W. Eikrem, S. Seoane, K. Smith, B. Edvardsen, A. Hofgaard, C. R. Tomas,  
974 New insights into the morphology and phylogeny of *Heterosigma akashiwo*  
975 (Raphidophyceae), with the description of *Heterosigma minor* sp. nov. *Phycologia* **55**, 279–  
976 294 (2016).

- 977 **31.** M. Wada, A. Miyazaki, T. Fujii, On the mechanisms of diurnal vertical migration  
978 behavior of *Heterosigma akashiwo* (Raphidophyceae). *Plant and cell physiology* **26**, 431-436  
979 (1985).
- 980 **32.** S. Hatano, Y. Hara, M. Takahashi, Photoperiod and nutrients on the vertical migratory  
981 behavior of a red tide flagellate, *Heterosigma akashiwo*. *J. Jpn. Phycol.* **31**, 263–269 (1983).
- 982 **33.** L. Arin, X. A. G. Morán, M. Estrada, Phytoplankton size distribution and growth rates in  
983 the Alboran Sea (SW Mediterranean): Short term variability related to mesoscale  
984 hydrodynamics. *J. Plankton Res.* **24**, 1019–1033 (2002).
- 985 **34.** J. L. Pinckney, C. R. Benitez-Nelson, R. C. Thunell, F. Muller-Karger, L. Lorenzoni, L.  
986 Troccoli, R. Varela, Phytoplankton community structure and depth distribution changes in the  
987 Cariaco Basin between 1996 and 2010. *Deep Sea Res Part 1 Oceanogr Res Pap.* **101**, 27–37  
988 (2015).
- 989 **35.** M. Latasa, A. M. Cabello, X. A. G. Morán, R. Massana, R. Scharek, Distribution of  
990 phytoplankton groups within the deep chlorophyll maximum. *Limnol Oceanogr.* **62**, 665–685  
991 (2017).
- 992 **36.** T. J. Smayda, Adaptations and selection of harmful and other dinoflagellate species in  
993 upwelling systems. 2. Motility and migratory behaviour. *Prog Oceanogr.* **85**, 71–91 (2010).
- 994 **37.** J.C. Beltrán-Rocha, C. Guajardo-Barbosa, H. Rodríguez-Fuentes *et al.*, Some  
995 implications of natural increase of pH in microalgae cultivation and harvest by  
996 autoflocculation. *Latin american journal of aquatic research* **49**, 836-842 (2021).
- 997 **38.** Z. Dubinsky and J. Rotem, Relations between algal populations and the pH of their  
998 media. *Oecologia* **16**, 53-60 (1974).
- 999 **39.** H. Kim, A. J. Spivack, S. Menden-Deuer, pH alters the swimming behaviors of the  
1000 raphidophyte *Heterosigma akashiwo*: Implications for bloom formation in an acidified ocean.  
1001 *Harmful Algae* **26**, 1–11 (2013).
- 1002 **40.** A. Vardi, D. Schatz, K. Beeri, U. Motro, A. Sukenik, A. Levine, A. Kaplan,  
1003 Dinoflagellate-cyanobacterium communication may determine the composition of  
1004 phytoplankton assemblage in a mesotrophic lake. *Current Biology* **12**, 1767–1772 (2002).
- 1005 **41.** J. D. Long, G. W. Smalley, T. Barsby, J. T. Anderson, M. E. Hay, Chemical cues induce  
1006 consumer-specific defenses in a bloom-forming marine phytoplankton. *Proc Natl Acad Sci U*  
1007 *S A.* **104**, 10512–10517 (2007).
- 1008 **42.** A. Vardi, F. Formiggini, R. Casotti, A. de Martino, F. Ribalet, A. Miralto, C. Bowler,  
1009 A stress surveillance system based on calcium and nitric oxide in marine diatoms. *PLoS Biol.*  
1010 **4**, 0411–0419 (2006).
- 1011 **43.** R. L. Golda, Assessing the influence of environmental pH on algal physiology using a  
1012 novel culture system. PhD thesis (2017).
- 1013 **44.** T. Masuda *et al.* Impact of Increased Nutrients and Lowered pH on Photosynthesis and  
1014 Growth of Three Marine Phytoplankton Communities From the Coastal South West Atlantic  
1015 (Patagonia, Argentina). *Fron. Marine Sci.* **8**, 609962 (2021).

- 1016 **45.** C.M. Duarte, I.E. Hendriks, T.S. Moore, *et al.*, Is ocean acidification an open-ocean  
1017 syndrome? Understanding anthropogenic impacts on seawater pH. *Estuaries and Coasts* **36**,  
1018 221-236 (2013).
- 1019 **46.** M. Dai, Z. Lu, W. Zhai *et al.*, Diurnal Variations of Surface Seawater pCO<sub>2</sub> in  
1020 Contrasting Coastal Environments. *Limnology and Oceanography* **54**, 735–745 (2009).
- 1021 **47.** G. Wang, J. Wenping, W. Shuling, X. Yi, *et al.*, Coastal Acidification Induced by Tidal-  
1022 Driven Submarine Groundwater Discharge in a Coastal Coral Reef System. *Environmental*  
1023 *Science & Technology* **48**, 13069–13075 (2014).
- 1024 **48.** S. Mukherjee, B. L. Bassler, Bacterial quorum sensing in complex and dynamically  
1025 changing environments. *Nature Reviews Microbiology* **17**, 371-382 (2019).
- 1026 **49.** N.A.M. Araújo, L.M.C. Janssen, T. Barois, *et al.*, Steering self-organisation through  
1027 confinement, *Soft Matter* **19**, 1695-1704 (2023).
- 1028 **50.** D. Schatz, A. Vardi, Extracellular vesicles—new players in cell–cell communication in  
1029 aquatic environments. *Current opinion in microbiology* **43**, 148-154 (2018).
- 1030 **51.** J. M. Diaz, S. Plummer, Production of extracellular reactive oxygen species by  
1031 phytoplankton: past and future directions. *J Plankton Res.* **40**, 655–666 (2018).
- 1032 **52.** X. Li, T. Liu, K. Wang, T. D. Waite, Light-induced extracellular electron transport by the  
1033 marine raphidophyte *Chattonella marina*. *Environ Sci Technol.* **49**, 1392–1399 (2015).
- 1034 **53.** K. Cho *et al.* Generation of reactive oxygen species (ROS) by harmful algal bloom  
1035 (HAB)-Forming phytoplankton and their potential impact on surrounding living organisms.  
1036 *Antioxidants* **11**, 206 (2022).
- 1037 **54.** R. Feely, A. Simone, N. Jan, *et al.*, The Combined Effects of Ocean Acidification,  
1038 Mixing, and Respiration on pH and Carbonate Saturation in an Urbanized Estuary. *Estuarine,*  
1039 *Coastal and Shelf Science* **88**: 442–449 (2010).
- 1040 **55.** A. M. Roberts, F. M. Deacon, Gravitaxis in motile micro-organisms: The role of fore-aft  
1041 body asymmetry. *J Fluid Mech.* **452**, 405–423 (2002).
- 1042 **56.** S. H. Koenig, Brownian motion of an ellipsoid. A correction to Perrin’s results.  
1043 *Biopolymers* **14**, 2421–2423 (1975).
- 1044 **57.** J. Happel, H. Brenner, Low Reynolds Number Hydrodynamics, Vol. 1 of Mechanics of  
1045 Fluids and Transport Processes (Springer Netherlands, 1981).
- 1046
- 1047
- 1048
- 1049
- 1050
- 1051

1052  
1053  
1054  
1055  
1056  
  
1057  
1058  
1059  
1060  
1061  
1062  
1063  
1064  
  
1065  
  
1066  
1067  
1068  
1069  
1070  
1071  
1072  
1073  
1074  
1075  
1076  
1077  
1078  
1079  
1080  
1081

## SUPPLEMENTARY MATERIAL

### **Phytoplankton tune local pH to actively modulate circadian swimming behavior**

Arkajyoti Ghoshal<sup>1</sup>, Jayabrata Dhar<sup>2</sup>, Hans-Peter Grossart<sup>3,4</sup>, and Anupam Sengupta<sup>1\*</sup>

<sup>1</sup>Physics of Living Matter, Department of Physics and Materials Science, University of Luxembourg, 162A, Avenue de la Faïencerie, L-1511 Luxembourg City, Luxembourg

<sup>2</sup>Department of Mechanical Engineering, National Institute of Technology Durgapur, 713203, India

<sup>3</sup>Department of Plankton and Microbial Ecology, Leibniz Institute of Freshwater Ecology and Inland Fisheries, Zur alten Fischerhuetten 2, 16775 Stechlin, Germany

<sup>4</sup>Institute of Biochemistry and Biology, Potsdam University, Maulbeerallee 2, D-14469 Potsdam, Germany

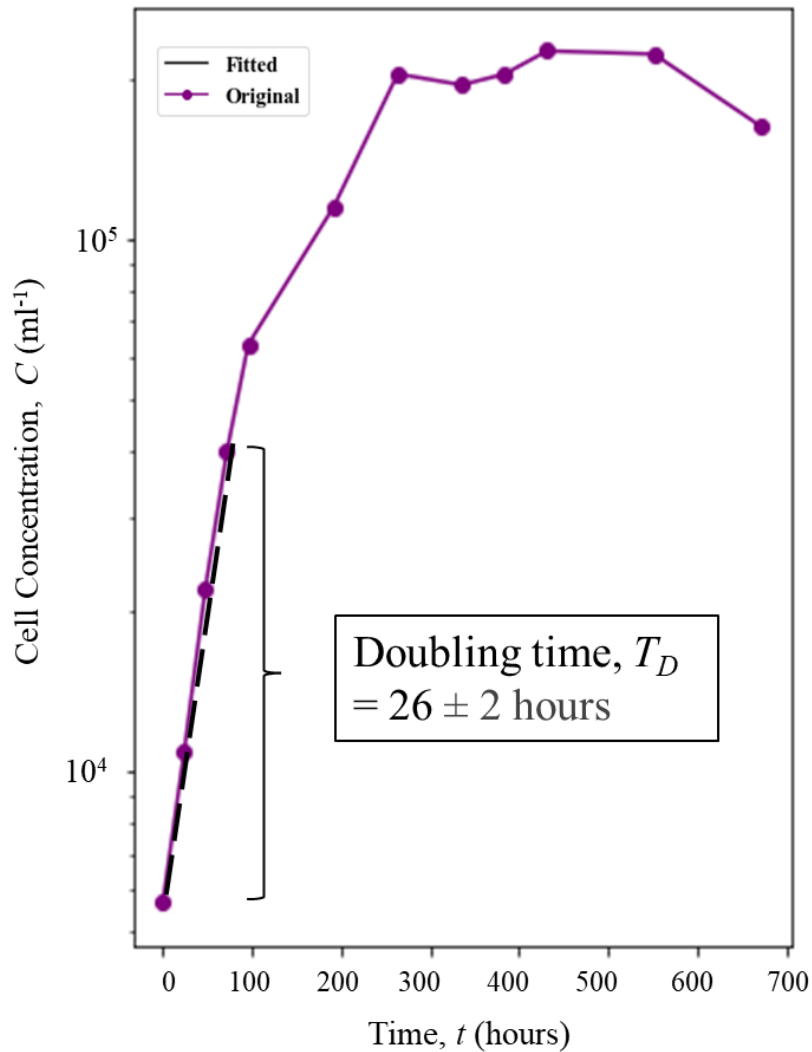
\* To whom correspondence should be addressed: [anupam.sengupta@uni.lu](mailto:anupam.sengupta@uni.lu)

#### **This file contains:**

Supplementary figures and captions for Figures S1 to S18

1082

## Supplementary Figures



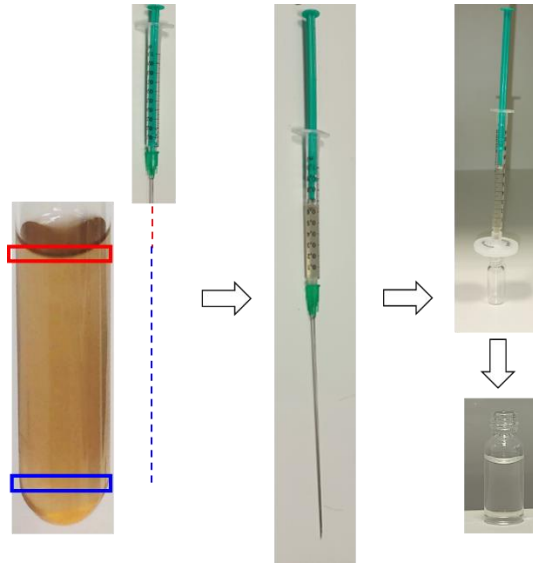
1083

1084

1085 **Fig. S1. Quantification of doubling time from HA 452 growth curve.** In order to compute  
1086 the doubling time, the growth curve shown in Fig.1 A (main text), was plotted in a logarithmic  
1087 scale, shown in purple. The exponential phase of growth is fitted to an exponential function  
1088 (shown in black lines). The coefficient of the exponent gives us the growth rate from which  
1089 doubling time is calculated (Materials and Methods). Doubling time,  $T_D$  ranges from 24 to 28  
1090 hours which matches well with ranges of other phytoplankton mentioned in literature (see main  
1091 text).

1092

1093

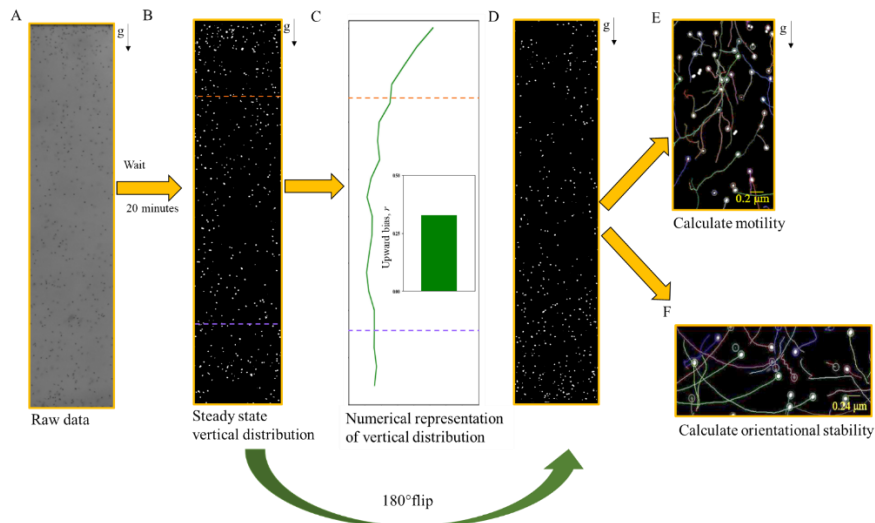


1094

1095

1096 **Fig. S2. Generation of filtrate from a cell culture.** To generate filtrates, cell samples are  
1097 collected from a growing culture (left most panel) from either the top (red box) or bottom  
1098 (blue box) region. Collection is done using a needle and syringe (Materials and Methods).  
1099 The red or blue dotted lines indicate the depth of needle for collection of top or bottom  
1100 sample. Once samples are collected (middle panel), they are passed through a 1  $\mu\text{m}$   
1101 sized syringe filter (right panel, top) and collected into a glass vial (right panel, bottom).  
1102 These are then used for measuring pH, nutrients, and response of cells in presence or absence  
1103 of same or opposite filtrates.

1104

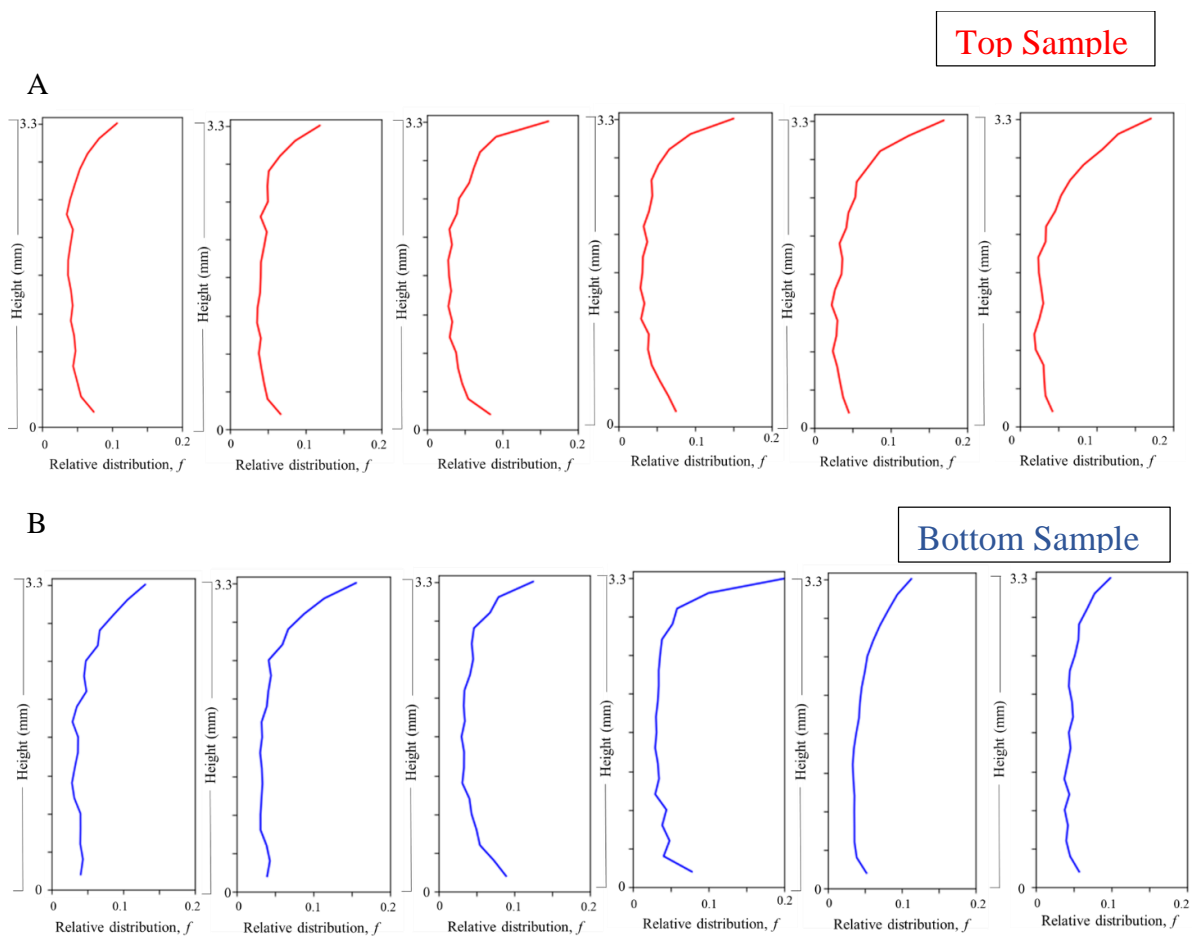


1105

1106 **Fig. S3. Image analysis pipeline.** This figure shows a general pipeline used for analyzing raw  
1107 data (panel (A)) and extract parameters like upward bias, motility and stability. These  
1108 parameters have been mentioned and used multiple times throughout the paper and uses the  
1109 same approach as shown here. First one takes the raw data and then binarizes it for downstream  
1110 analyses. (B) shows one such binarized image of cells in a millifluidic chamber, after 20  
1111 minutes from the point of insertion. (C) shows how the binarized input is used to compute

1112 vertical distribution, shown in green line (for details, see Materials and methods). From this,  
1113 upward bias value is calculated by considering the cell concentration in the top and bottom  
1114  $1/5^{\text{th}}$  of the chamber, indicated by the dark orange and lavender dotted lines. **(D)** To calculate  
1115 motility and orientational stability, after an equilibration time (here 20 minutes), the chamber  
1116 is flipped by 180 degrees. Cells at the top pre-flip are now at the bottom and start to swim up.  
1117 **(E)** As cells swim up, a short video is captured which is analysed to obtain swimming  
1118 trajectories from which motility parameter like speed and swimming direction can be obtained  
1119 for individual cells. **(F)** Flipping the chamber also changes cellular orientation from their stable  
1120 configuration and they start to reorient, as shown by the arc-like trajectories.

1121



1122

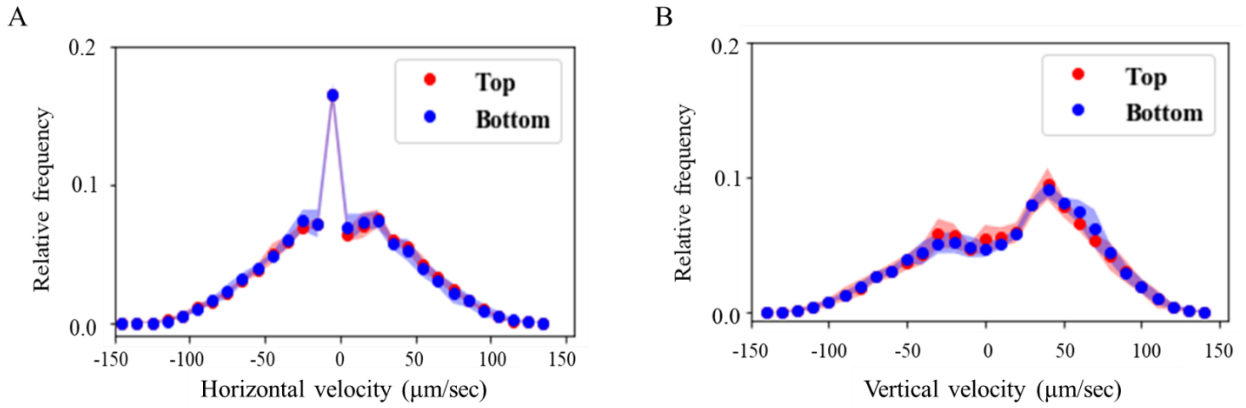
1123 **Fig. S4. Vertical distribution of cells in a multifluidic chamber.** To observe the vertical  
1124 distribution of cells, samples were collected from top (red) and bottom (blue) and placed into  
1125 a multifluidic chamber of vertical height 3.3 mm. After 20 minutes, the entire height was  
1126 imaged for subsequent cell count. **(A)** shows the distribution of top cells with each panel  
1127 corresponding to one replicate (of 6 replicates, 3 biological replicates each having 2 technical  
1128 replicates). **(B)** shows the same but for bottom cells. First two panels show technical replicates  
1129 of the first biological replicate and the rest follows that order.

1130

1131

1132

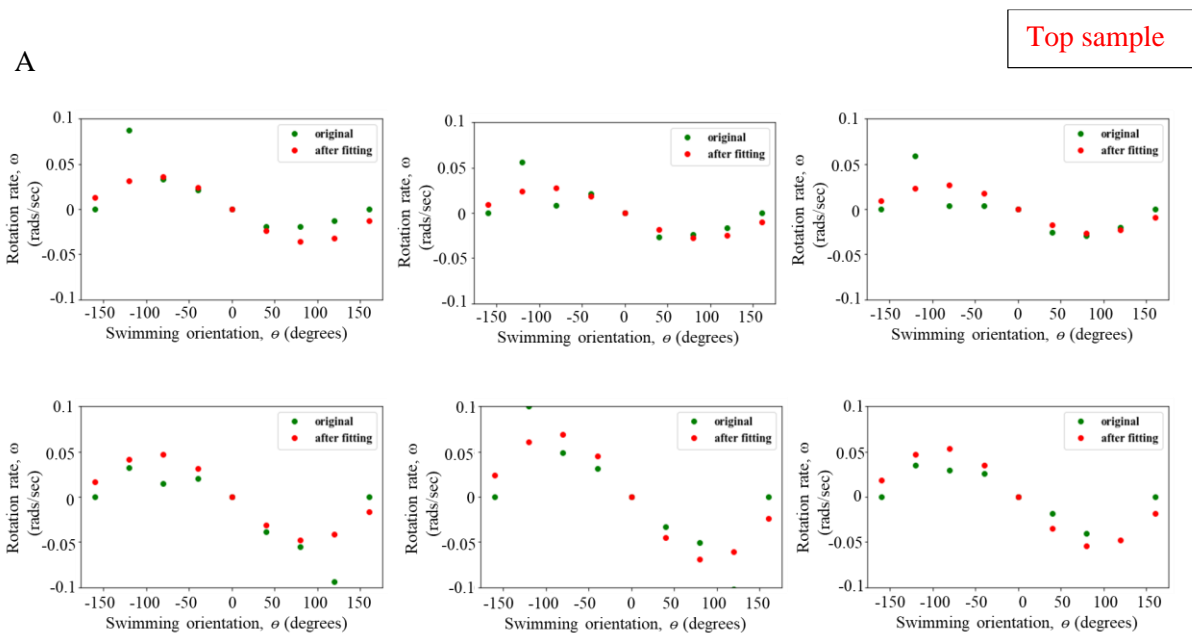




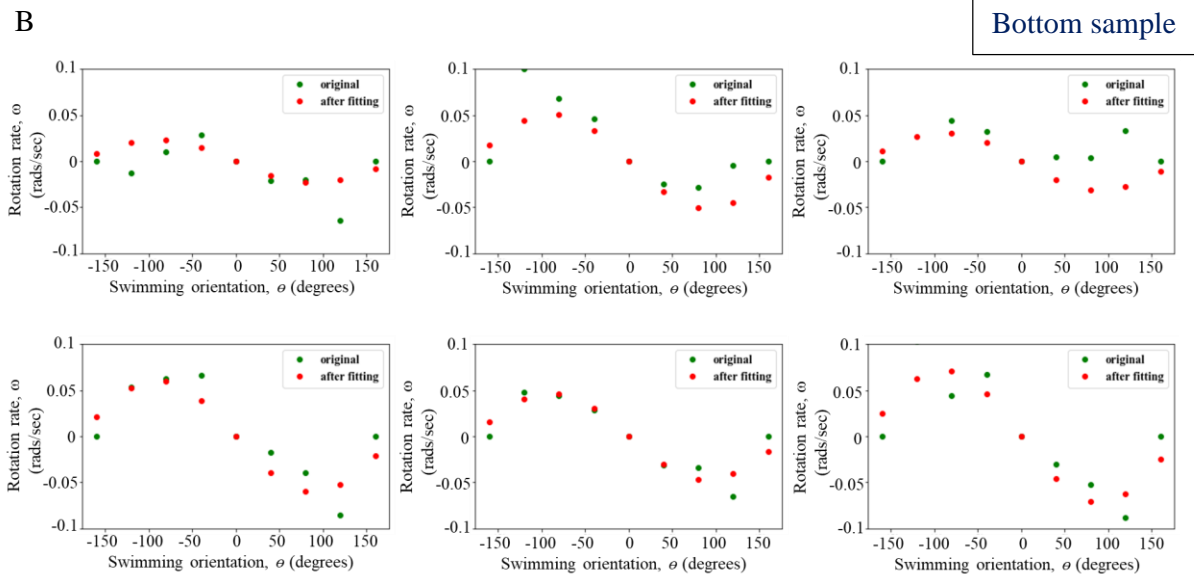
1133

1134 **Fig. S5. Motility parameters of cells.** While Fig. 1 H of main text shows that the mean  
 1135 absolute swimming speed of top and bottom cells are similar, we also wanted to see if their  
 1136 directionality remains similar identical as well (reason in main text). **(A)** shows the relative  
 1137 distribution of mean horizontal swimming speed of all 6 replicates for top and bottom cells (red  
 1138 and blue respectively). Horizontal velocity is divided into two sections about 0. Cells  
 1139 swimming towards their right from their initial position is assigned positive velocity and those  
 1140 swimming left are assigned negative velocities. Results indicate that the majority population  
 1141 of both samples have a mean horizontal speed of 0  $\mu\text{m}/\text{s}$ , meaning that on a population scale,  
 1142 cells do not show much displacement in the horizontal direction. **(B)** shows the relative  
 1143 distribution of mean vertical swimming speed of the same. Vertical velocity is divided into two  
 1144 sections about 0. Cells swimming against gravity from their initial position is assigned positive  
 1145 velocity and those swimming towards, are assigned negative velocities. (Direction of gravity,  
 1146  $g$ , is shown by the black arrows to the right of both panels) Mean vertical velocity of both  
 1147 samples peak at around 35  $\mu\text{m}/\text{s}$ , meaning that the population as a whole move actively against  
 1148 gravity, precisely in the negative vertical direction.

1149



1150



1151

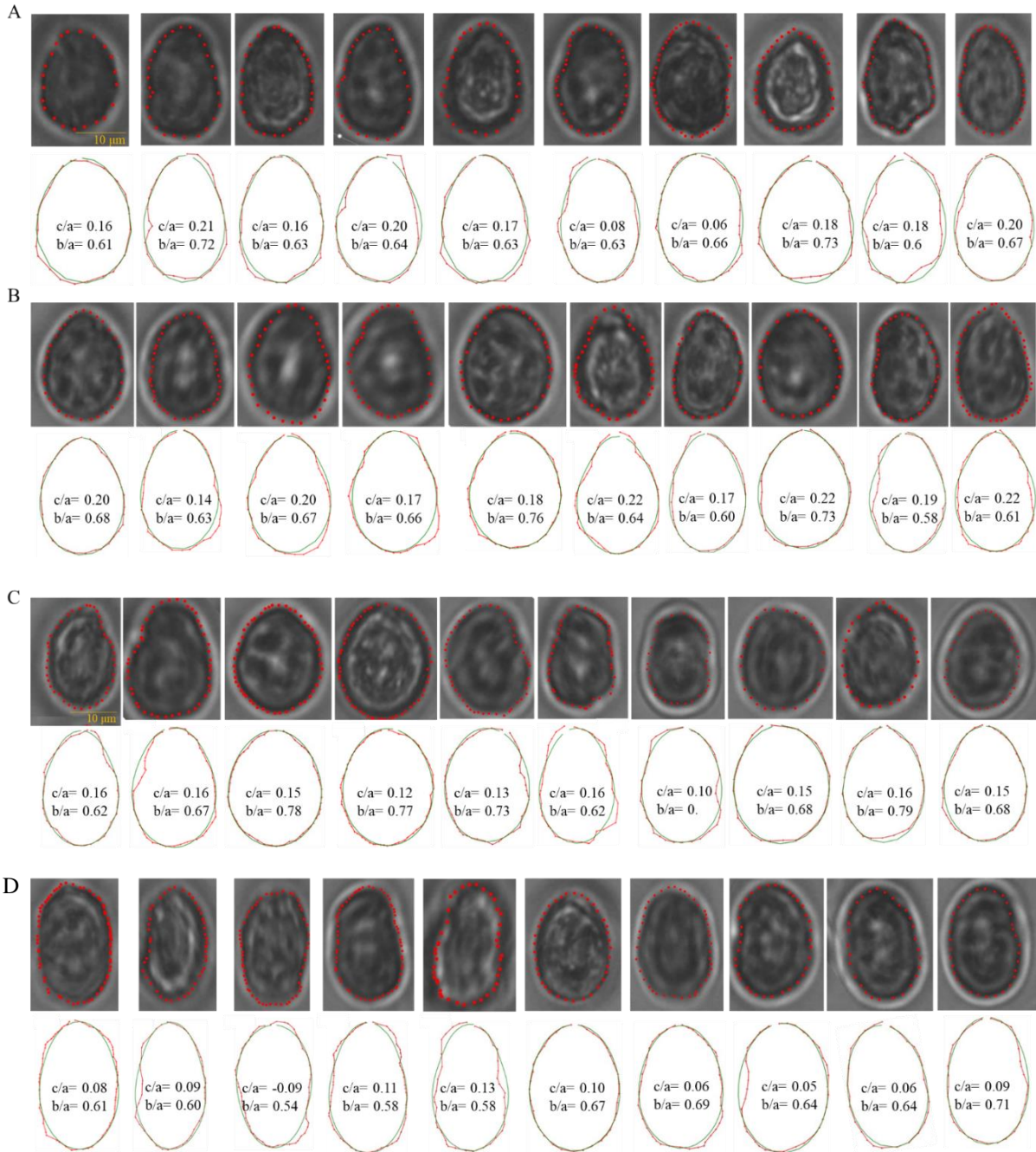
1152 **Fig. S6. Quantification of the orientational stability of cell samples.** To compute the stability of  
 1153 top and bottom samples, rotation rate ( $\omega$ ) of cells were plotted as a function of the instantaneous  
 1154 angular direction ( $\theta$ ). The time of experiment was day (11 hours). (A) shows the stability of top  
 1155 cells with each panel corresponding to one replicate. Red dots correspond to experimental data  
 1156 and green dots to the sinusoidal curve obtained by fitting a sinusoid to the experimental data.  
 1157 (B) shows the same but for bottom cells. The amplitude,  $A$  of the fitted curve was used to obtain  
 1158 the reorientation timescale,  $B$  as  $B = \frac{1}{2A}$ . Note that there are 12 replicates: 3 biological replicates  
 1159 x 2 technical replicates x 2 subreplicates, where 1 subreplicate is obtained by imaging 1  
 1160 technical replicate for two consecutive flips, as detailed in the Materials and methods section.  
 1161 Here the subreplicates per technical replicate has been combined together, thus showing a total  
 1162 of  $3 \times 2 \times 1 = 6$  plots.

1163

1164

1165

1166

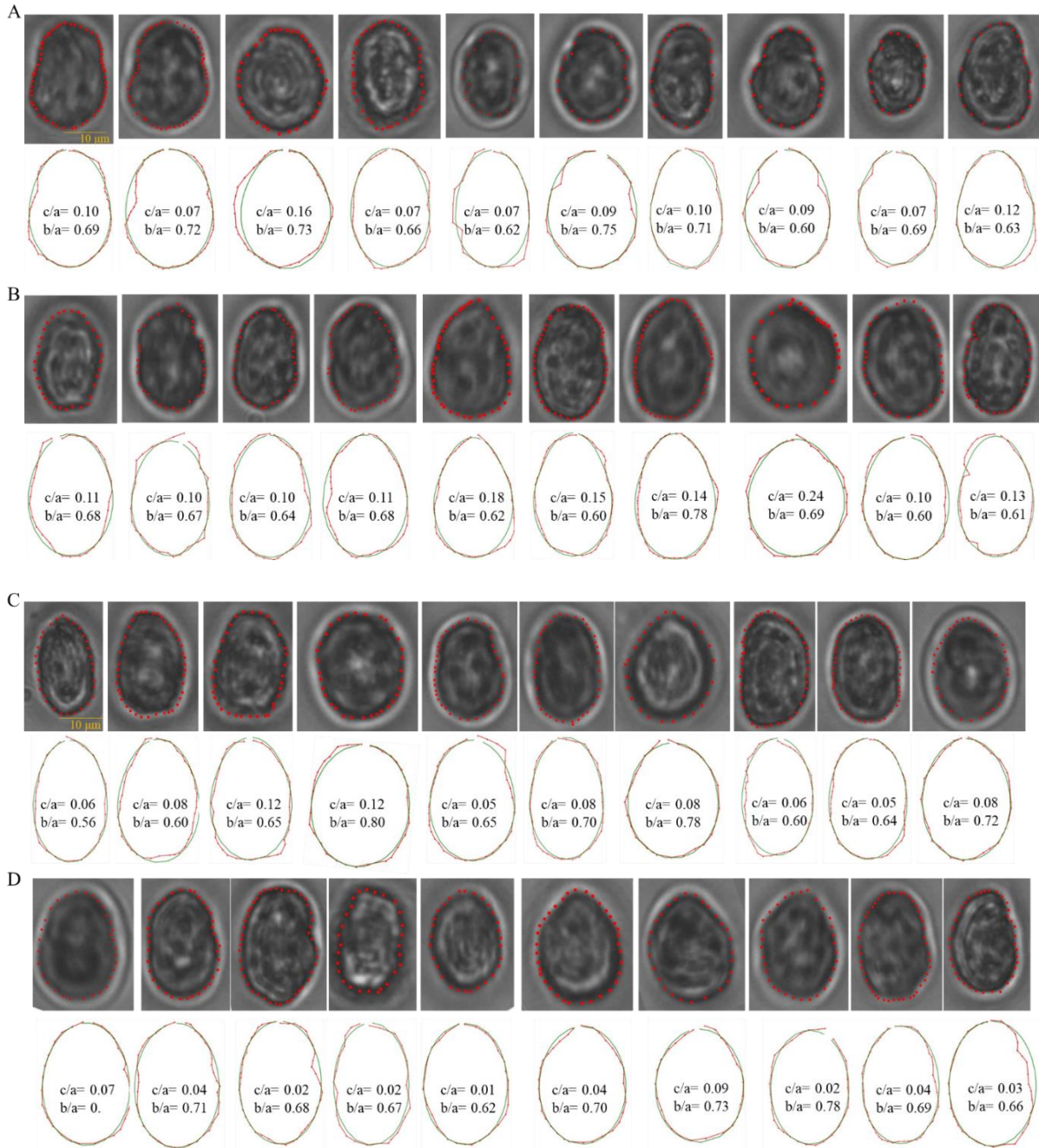


1167

1168

1169 **Fig. S7. Quantification of morphological parameters of top cells.** The top row of each panel  
 1170 shows phase contrast images of top cells ( $N = 10$ ). The external contour of each cell was  
 1171 marked, and co-ordinates were extracted. These were then fed into an image analysis pipeline  
 1172 to fit each contour with a fore-aft asymmetric ellipse. The  $c/a$  parameter is a quantification of  
 1173 this asymmetry. Panels A to D represents distinct time points of 0, 20, 60 and 120 min.

1174

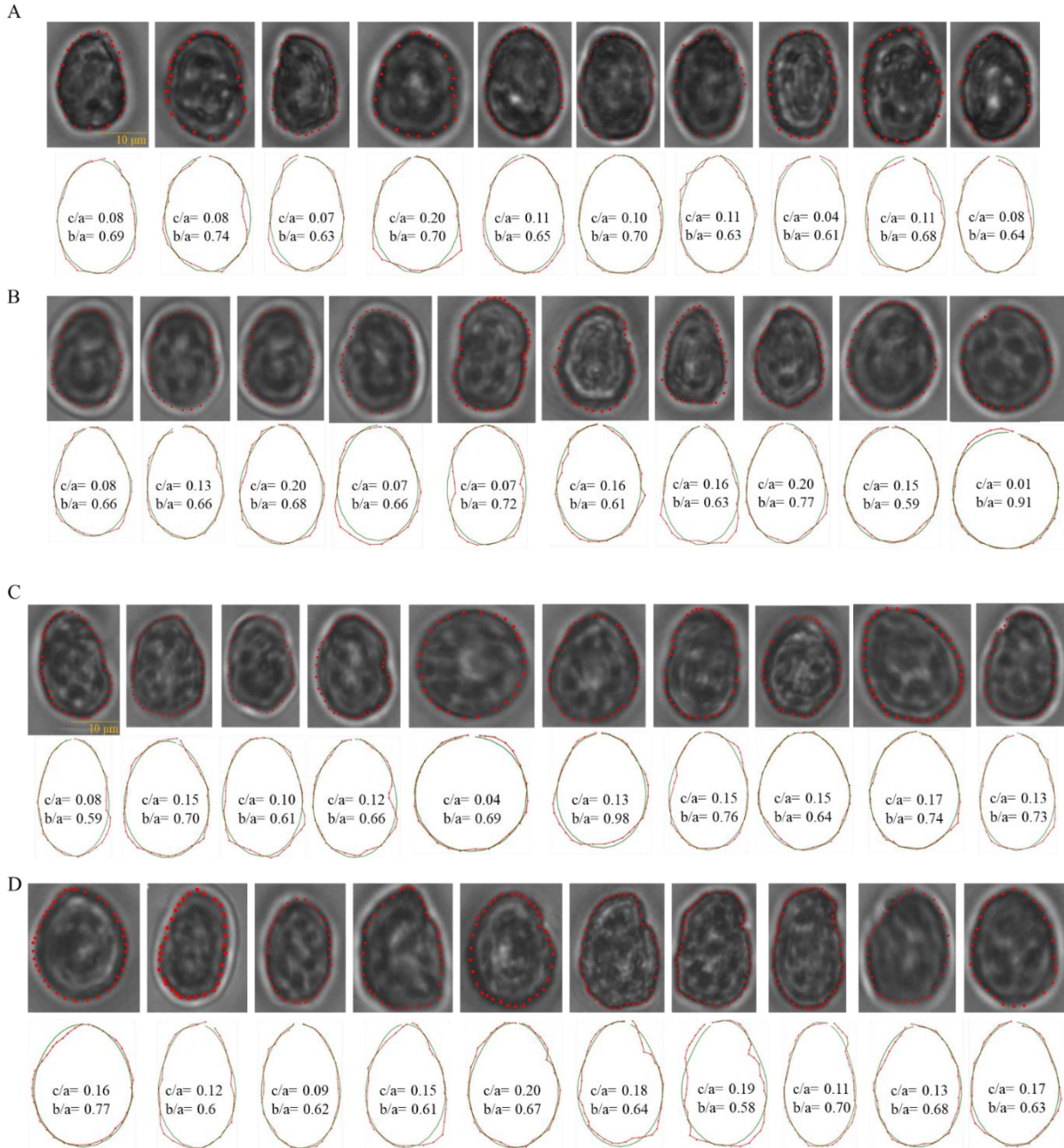


1175

1176

1177 **Fig. S8. Quantification of morphological parameters of bottom cells.** The top row of each  
1178 panel shows phase contrast images of bottom cells ( $N = 10$ ). The external contour of each cell  
1179 was marked, and co-ordinates were extracted. These were then fed into an image analysis  
1180 pipeline to fit each contour with a fore-aft asymmetric ellipse. The  $c/a$  parameter is a  
1181 quantification of this asymmetry. Panels A to D represents distinct time points of 0, 20, 60 and  
1182 120 min.

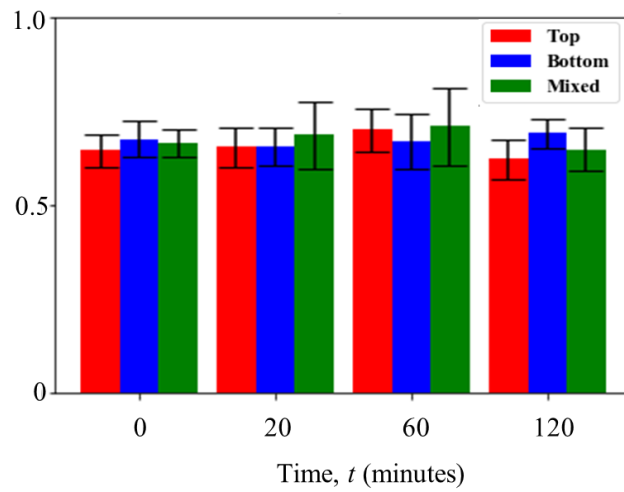
1183



1184

1185

1186 **Fig. S9. Quantification of morphological parameters of mixed cells.** The top row of each  
1187 panel shows phase contrast images of 50:50 mixed cells ( $N = 10$ ). The external contour of each  
1188 cell was marked, and co-ordinates were extracted. These were then fed into an image analysis  
1189 pipeline to fit each contour with a fore-aft asymmetric ellipse. The  $c/a$  parameter is a  
1190 quantification of this asymmetry. Panels A to D represents distinct time points of 0, 20, 60 and  
1191 120 min.

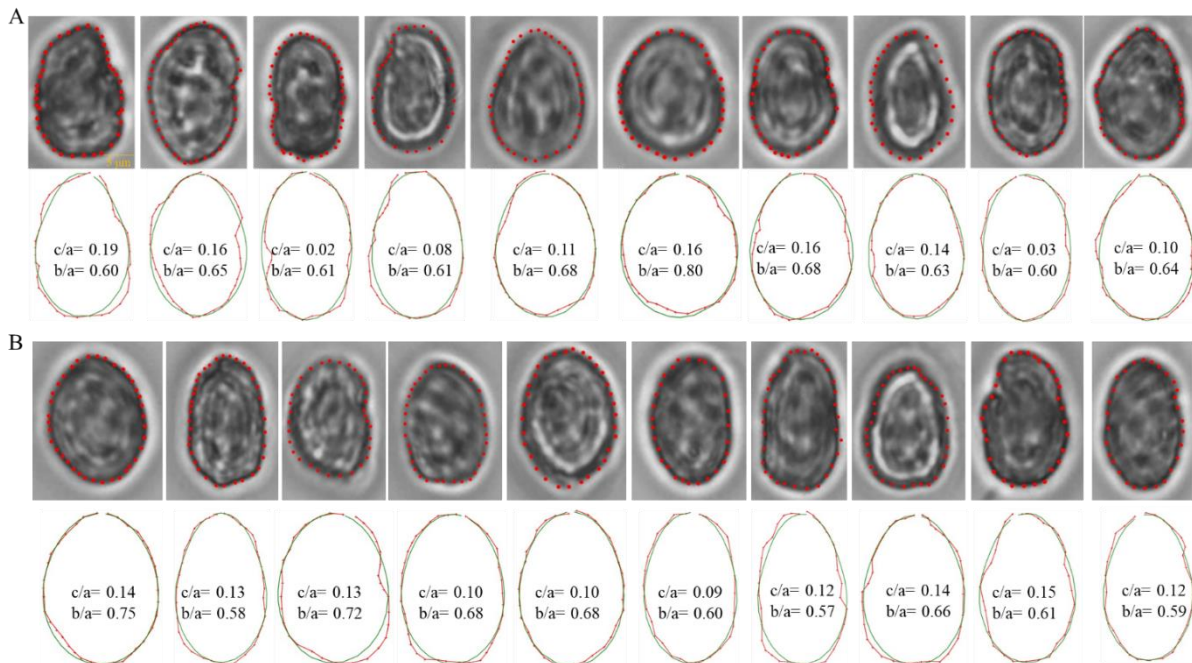


1192  
1193  
1194  
1195  
1196  
1197  
1198  
1199  
1200

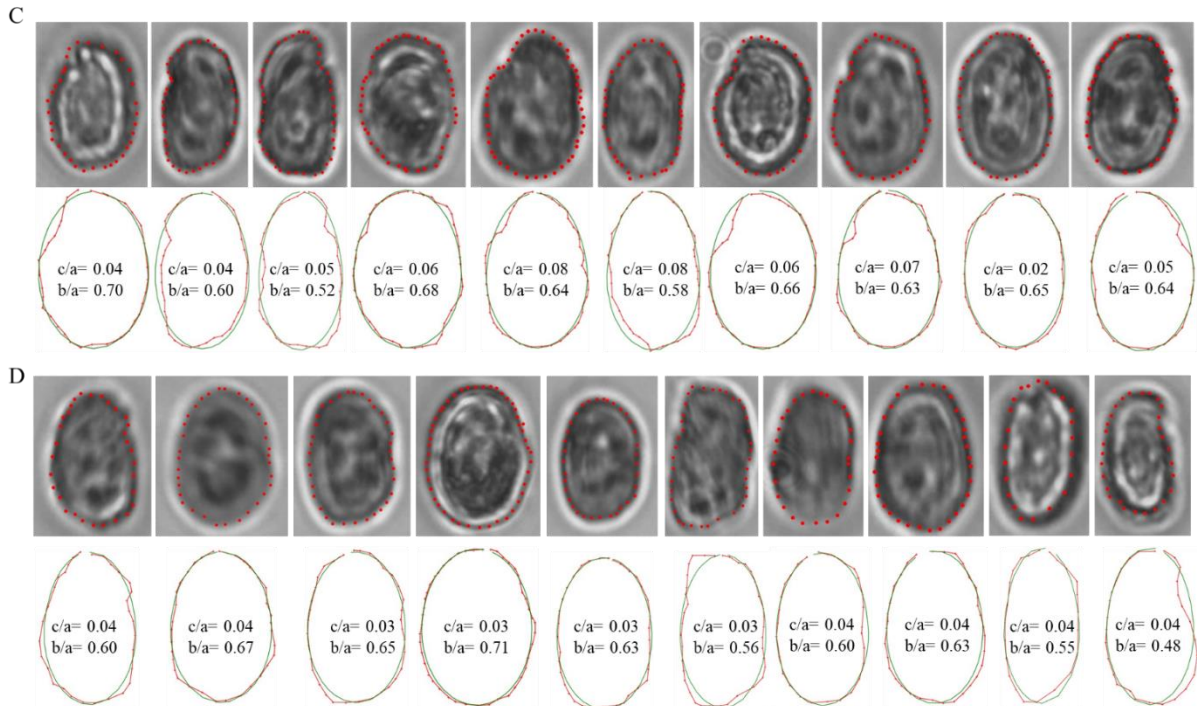
**Fig. S10.  $b/a$  values of cells over time.** Complementing the  $c/a$  values shown in main text, this figure shows the  $b/a$  values, the ratio of the minor to major semi axis, that gives an idea of the shape of cells. A value of 0 means cells are highly asymmetric, while that of 1 means highly rounded cells. For top cells (red bar), the mean ( $\pm$  s.d.) values over 0, 20, 60 and 120 minutes are  $0.65 \pm 0.04$ ,  $0.66 \pm 0.05$ ,  $0.7 \pm 0.06$  and  $0.62 \pm 0.05$ . For bottom cells (blue bar), they are  $0.68 \pm 0.05$ ,  $0.66 \pm 0.05$ ,  $0.67 \pm 0.07$  and  $0.7 \pm 0.04$ . For mixed cells (green bar), they are  $0.66 \pm 0.04$ ,  $0.69 \pm 0.09$ ,  $0.7 \pm 0.1$  and  $0.65 \pm 0.06$ .

Top cells + Top filtrate (TT)

1201



1202



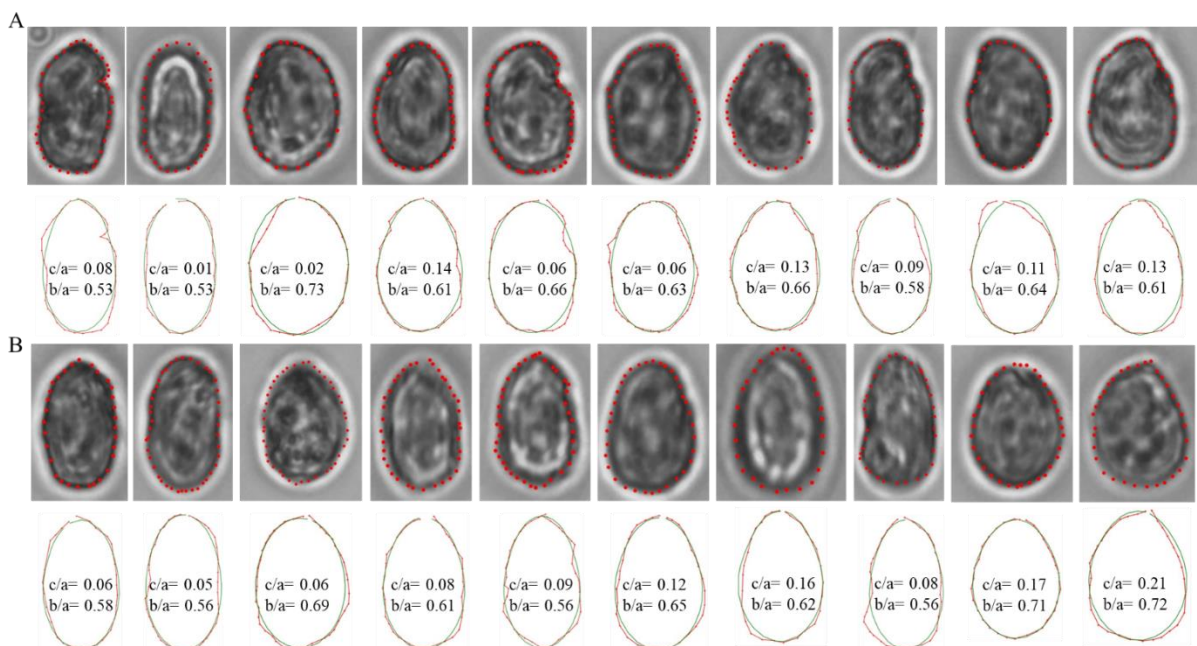
1203

1204 **Fig. S11. Quantification of morphological parameters of top cells in top filtrate [T, T].** The  
 1205 top row of each panel shows phase contrast images of top cells in presence of top filtrate ( $N =$   
 1206  $10$ ). The external contour of each cell was marked, and co-ordinates were extracted. These  
 1207 were then fed into an image analysis pipeline to fit each contour with a fore-aft asymmetric  
 1208 ellipse. The  $c/a$  parameter is a quantification of this asymmetry. Panels A to D represents  
 1209 distinct time points of 0, 20, 60 and 120 min.

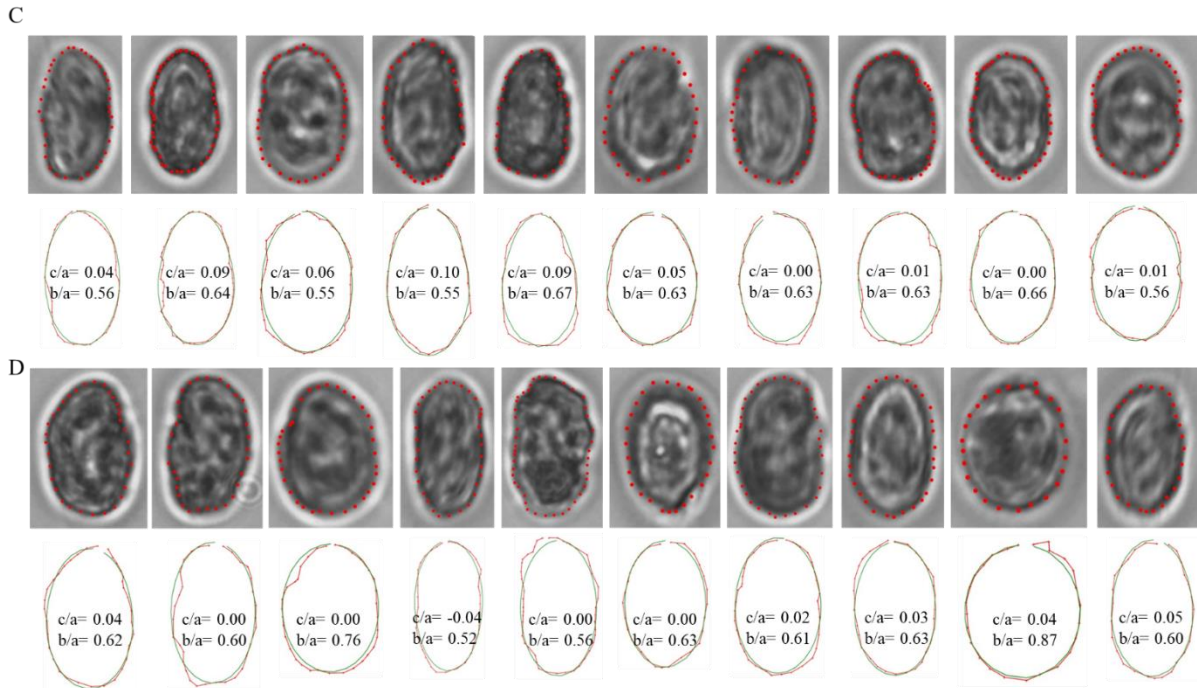
1210

Bottom cells + bottom filtrate (BB)

1211



1212



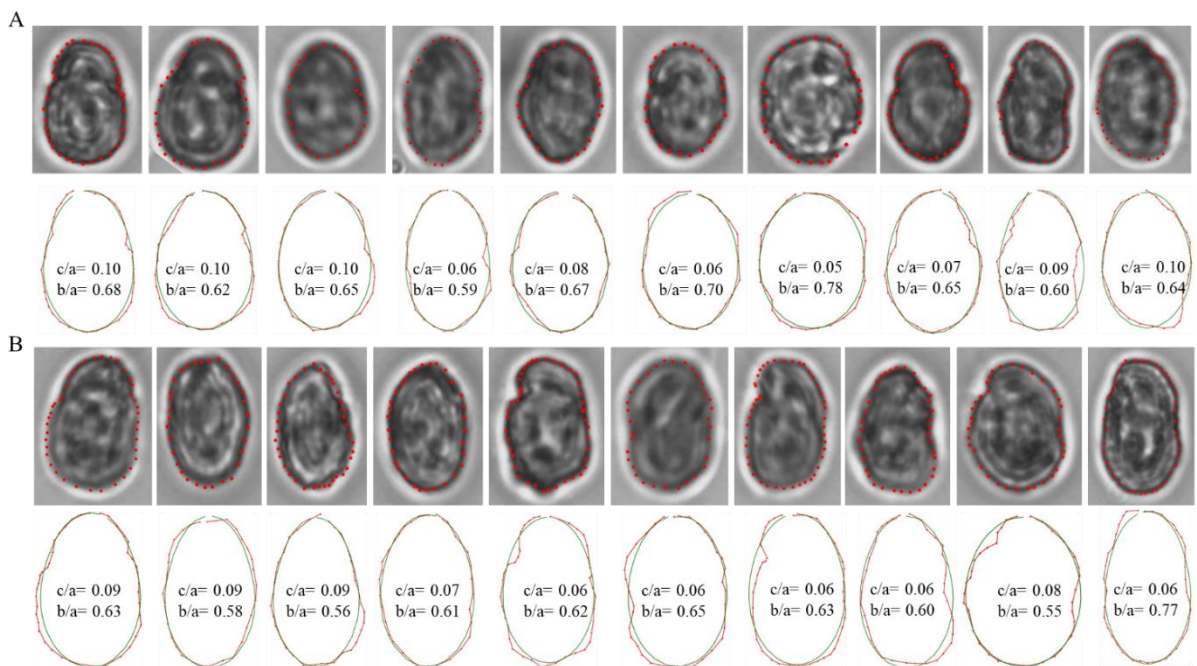
1213

1214 **Fig. S12. Quantification of morphological parameters of bottom cells in bottom filtrate**  
 1215 **[B, B].** The top row of each panel shows phase contrast images of top cells in presence of top  
 1216 filtrate ( $N = 10$ ). The external contour of each cell was marked, and co-ordinates were  
 1217 extracted. These were then fed into an image analysis pipeline to fit each contour with a fore-  
 1218 aft asymmetric ellipse. The  $c/a$  parameter is a quantification of this asymmetry. Panels A to D  
 1219 represents distinct time points of 0, 20, 60 and 120 min.

1220

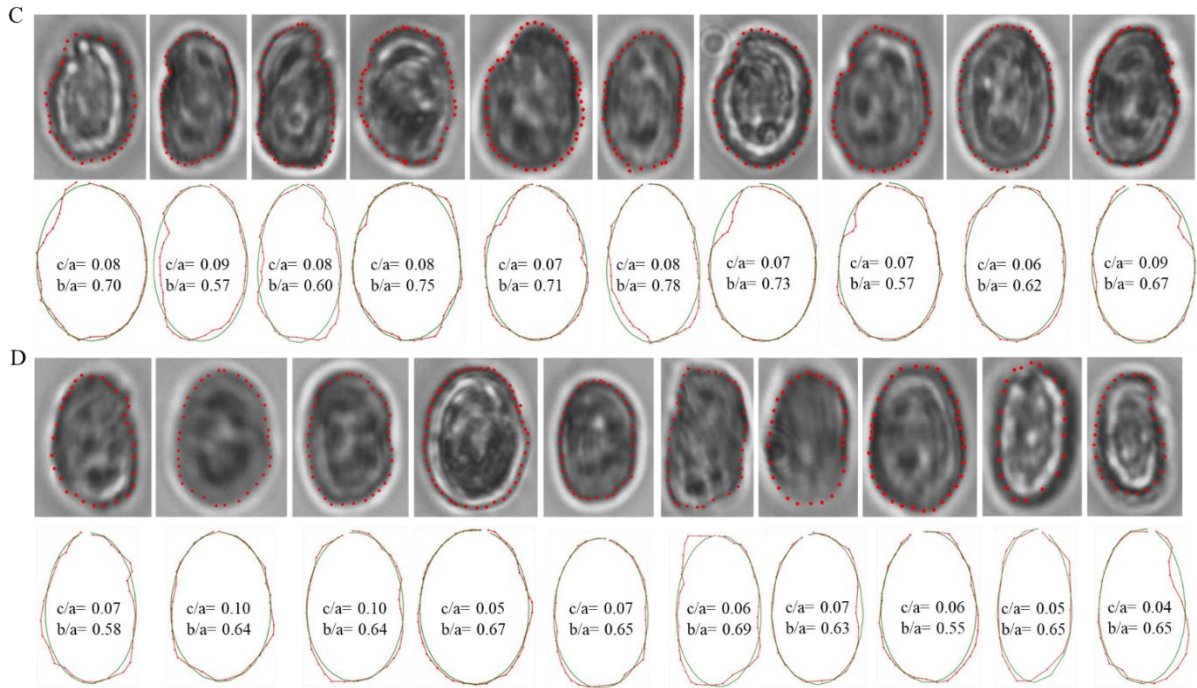
Top cells + Bottom filtrate (BT)

1221



1222



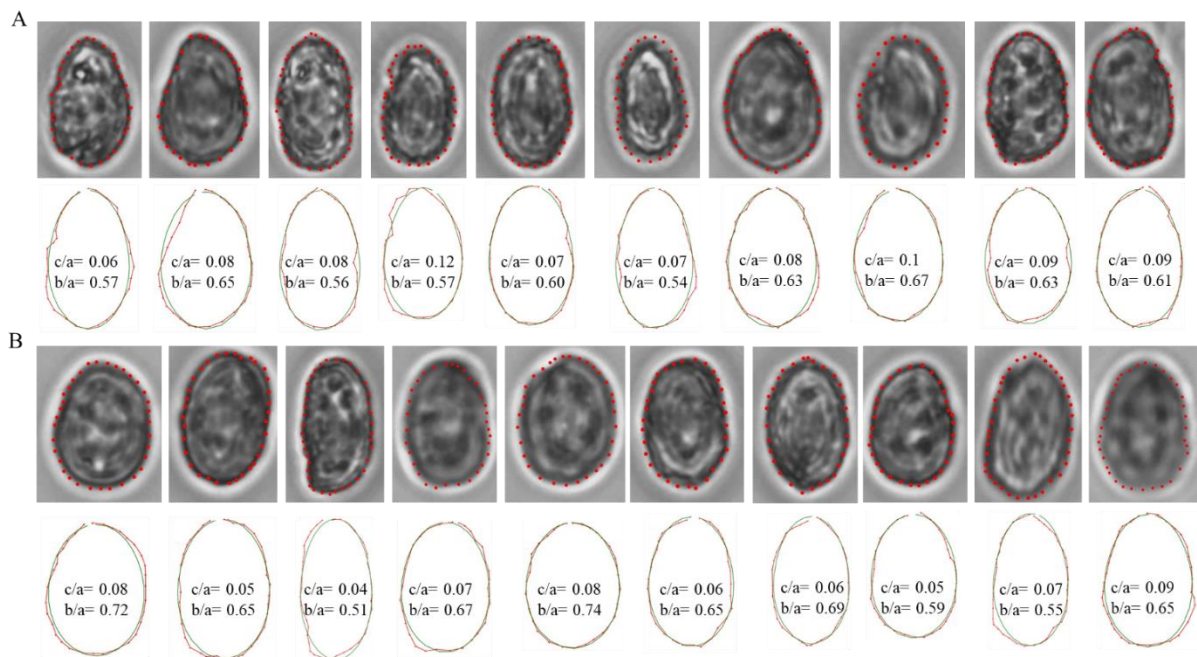


1223

1224 **Fig. S13. Quantification of morphological parameters of top cells in bottom filtrate [B,**  
 1225 ***T*].** The top row of each panel shows phase contrast images of top cells in presence of top  
 1226 filtrate ( $N = 10$ ). The external contour of each cell was marked, and co-ordinates were  
 1227 extracted. These were then fed into an image analysis pipeline to fit each contour with a fore-  
 1228 aft asymmetric ellipse. The  $c/a$  parameter is a quantification of this asymmetry. Panels A to D  
 1229 represents distinct time points of 0, 20, 60 and 120 min.

1230

Bottom cells + Top filtrate (*TB*)



1231

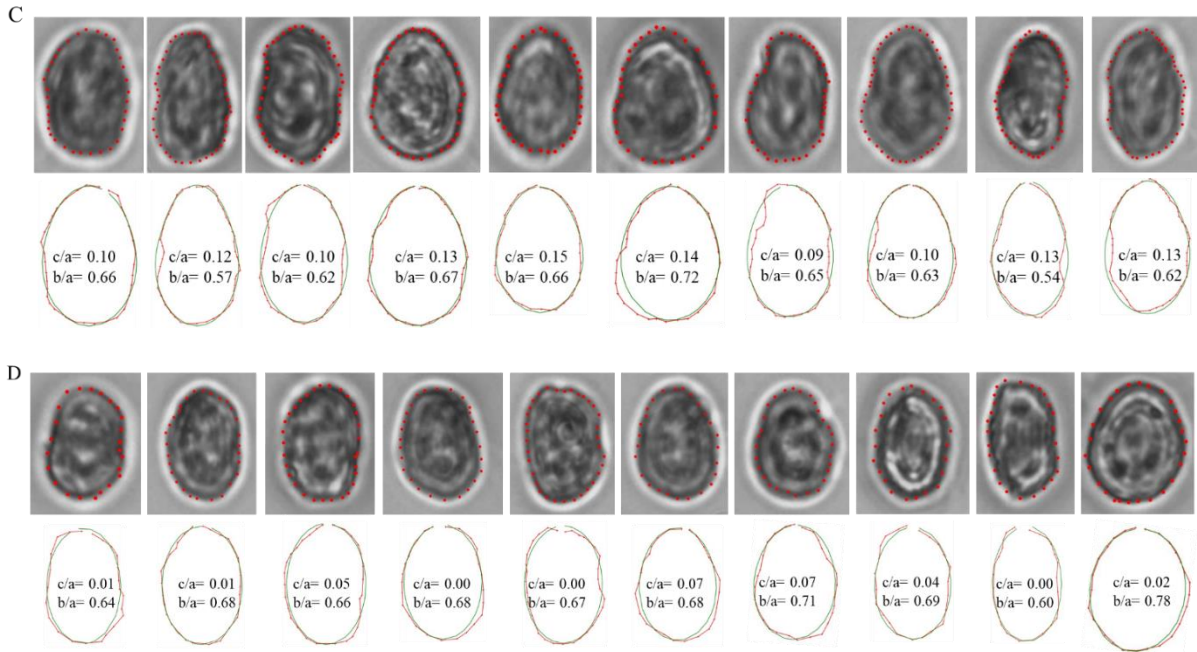


**Fig. S14. Quantification of morphological parameters of bottom cells in top filtrate [T, B].**

The top row of each panel shows phase contrast images of top cells in presence of top filtrate ( $N = 10$ ). The external contour of each cell was marked, and co-ordinates were extracted. These were then fed into an image analysis pipeline to fit each contour with a fore-aft asymmetric ellipse. The  $c/a$  parameter is a quantification of this asymmetry. Panels A to D represents distinct time points of 0, 20, 60 and 120 min.

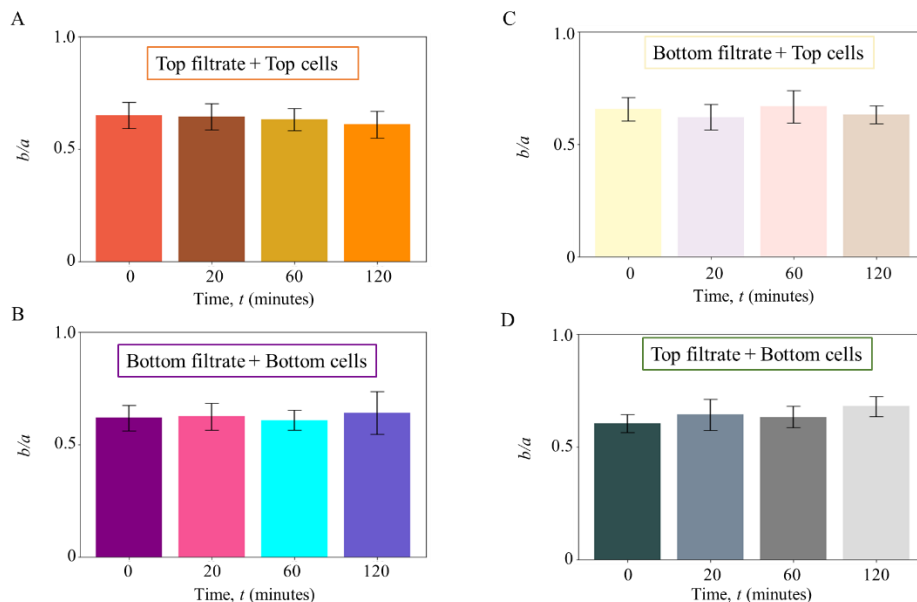
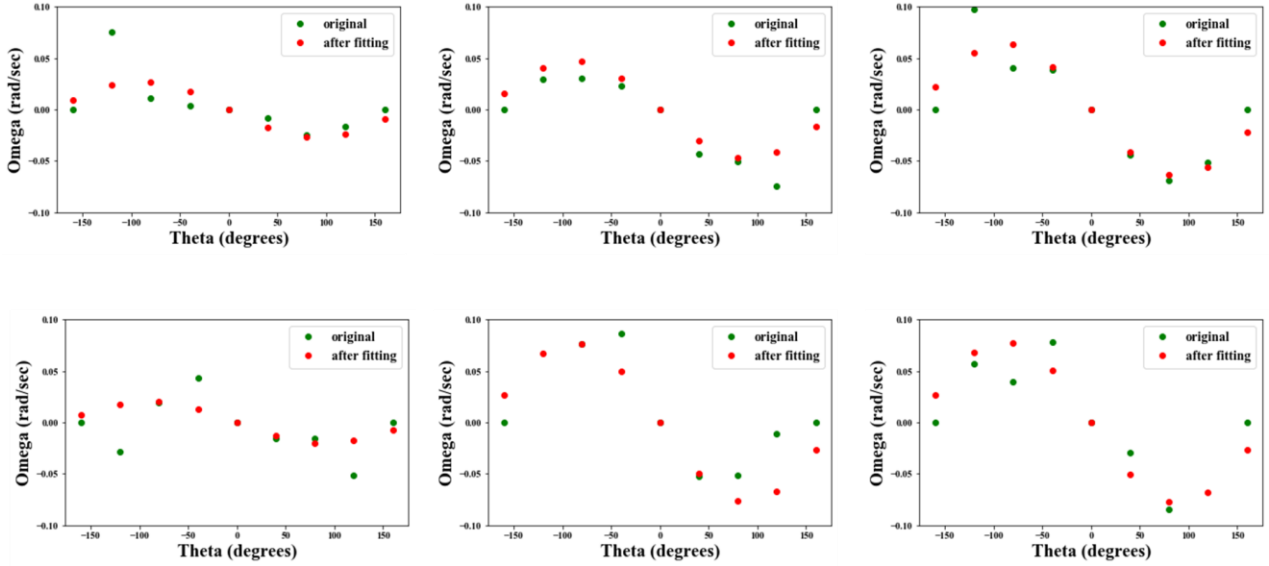


**Fig. S15.  $b/a$  values of cells over time in presence of filtrates. (A)** For top cells in presence of top filtrate [T, T], the mean ( $\pm$  s.d.) values of  $b/a$  over 0, 20, 60 and 120 minutes are  $0.65 \pm 0.06$ ,  $0.64 \pm 0.06$ ,  $0.63 \pm 0.05$  and  $0.61 \pm 0.06$ . **(B)** For bottom cells in presence of bottom filtrate [B, B], the mean ( $\pm$  s.d.) values are  $0.62 \pm 0.06$ ,  $0.62 \pm 0.06$ ,  $0.61 \pm 0.05$  and  $0.64 \pm 0.1$ . **(C)** For top cells in presence of bottom filtrate [B, T], the mean ( $\pm$  s.d.) values are  $0.66 \pm 0.05$ ,

1248  $0.62 \pm 0.06$ ,  $0.67 \pm 0.07$  and  $0.63 \pm 0.04$ . **(D)** For bottom cells in presence of top filtrate  $[T, B]$ ,  
 1249 the mean ( $\pm$  s.d.) values are  $0.6 \pm 0.04$ ,  $0.64 \pm 0.07$ ,  $0.63 \pm 0.05$  and  $0.68 \pm 0.04$ .

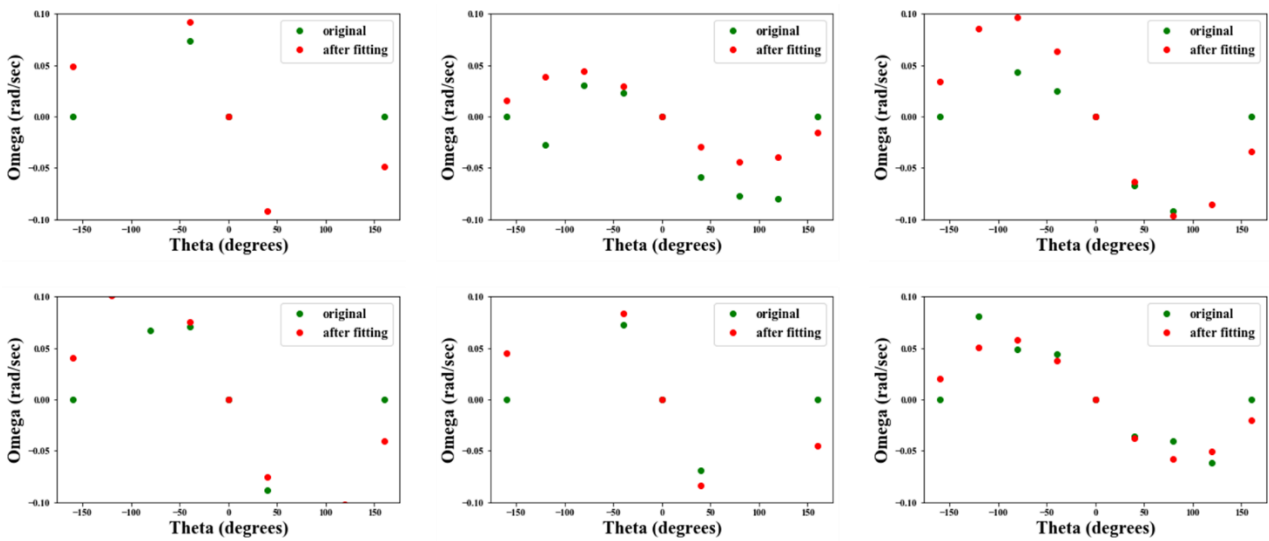
1250  
 1251  
 1252  
 1253

A



1254

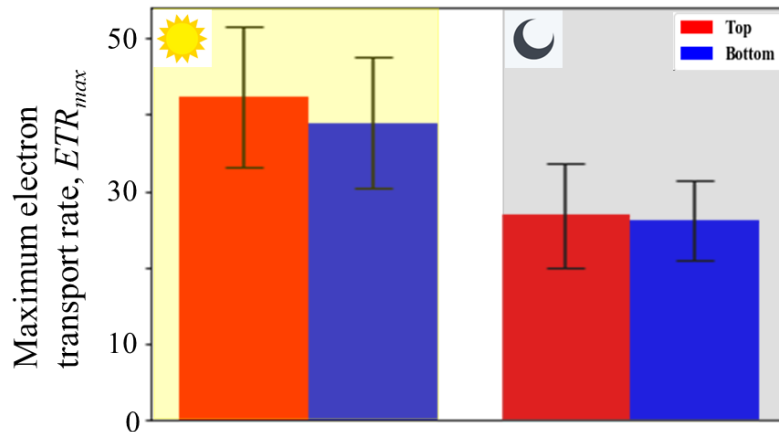
B



1256

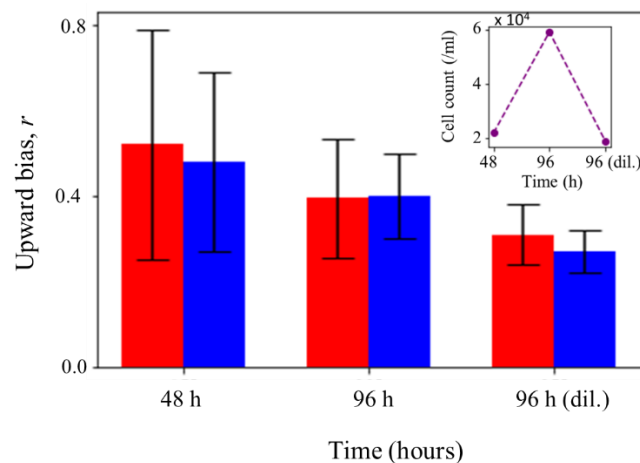
1257

1258 **Fig. S16. Quantification of the orientational stability of cell samples during night.** To compute  
 1259 the stability of top and bottom samples, rotation rate ( $\omega$ ) of cells were plotted as a function of the  
 1260 instantaneous angular direction ( $\theta$ ). The time of experiment was 00:00 h. **(A)** shows the stability  
 1261 of top cells with each panel corresponding to one replicate (of 6 replicates, as mentioned in  
 1262 Fig. S3). Red dots correspond to experimental data and green dots to the sinusoidal curve  
 1263 obtained by fitting a sinusoid to the experimental data. **(B)** shows the same but for bottom cells.  
 1264 The amplitude,  $A$  of the fitted curve was used to obtain the reorientation timescale,  $B$  as  $B = \frac{1}{2A}$ .  
 1265



1266  
1267  
1268  
1269  
1270  
1271  
1272  
1273  
1274  
1275

**Fig. S17. Estimation of the electron transport rate ( $ETR_{max}$ ) using the PAM device.** Complementing the maximum photosynthetic yield and non-photochemical quenching, two key processes during light harvesting, this figure shows the maximum ETR,  $ETR_{max}$ , during the same. During daytime, the difference between top and bottom for this value is not statistically significant ( $p = 0.69$ ). At night as well, there is no significant difference ( $p = 0.94$ ).



1276  
1277  
1278  
1279  
1280  
1281  
1282  
1283  
1284  
1285

**Fig. S18. Effect of cell concentration on swimming behavior.** To study the effect of concentration on population behavior, two points in growth phase: 48 h and 96 h were chosen for which the upward bias ( $r$ ) values were measured (cell counts are shown in the inset). At 48 h, both top (red bar) and bottom (blue bar) have higher mean ( $\pm$  s.d.)  $r$  than at 96 h. Same cells from 96-hour culture were taken and diluted (dil.)  $\sim 3$  times with corresponding filtrate, to achieve a concentration comparable to that at 48 h (third data point, inset). The  $r$  value of this diluted sample was calculated and compared to the other two datasets. 4 replicates were used for 48 h and 96 h (diluted), and 6 at the 96 h timepoint.